Spectral iInduced pPolarization survey for the estimation of hydrogeological parameters in an active rock glacier

Clemens Moser[1], Umberto Morra di Cella[2], Christian Hauck[3], and Adrián Flores Orozco[1]

[1]Research Unit Geophysics, Department of Geodesy and Geoinformation, TU Wien, Vienna, Austria
[2]Climate Change Unit, ARPA VdA (Environmental Protection Agency of Valle d'Aosta), Aosta valley, Italy
[3]Department of Geosciences, University of Fribourg, Fribourg, Switzerland

Correspondence to: Clemens Moser (clemens.moser@geo.tuwien.ac.at)

Abstract. Degrading permafrost in rock glaciers has been reported from several sites in the European Alps. Changes in ground temperature and ice content are expected to affect the hydrogeological properties of the rock glacier and in turn modify the runoff regime and groundwater recharge in high-mountain environments. In this study, we investigate the use of an emerging geophysical method in permafrost studies to understand the hydrogeological properties of the active Gran Sometta rock glacier, which consists of a two lobe-tongue (a white and a black) differing in their geologies. We present the application of the spectral induced polarization (SIP) imaging, a method that provides quasi-continuous spatial information about the electrical conductivity and polarization of the subsurface, which are linked to hydrogeological properties. To quantify the water content and the hydraulic conductivity from SIP imaging results, we used the petrophysical dynamic stern layer model. The SIP results show a continuously frozen layer at 4-6 m depth along both lobes which hinders the infiltration of water leading to a quick flow through the active layer. To evaluate our results, we conducted tracer experiments monitored with a time-lapse electrical conductivity imaging which confirms the hydraulic barrier associated with the frozen layer and allows to quantify the pore water velocity (~10^{-2} m/s). Below the frozen layer, both lobes have distinct water content and hydraulic conductivity. We observed a higher water content in the black lobe, which moves faster than the white lobe supporting the hypothesis that the water content at the shear horizon ~~dominates~~ affects the rock glacier velocity. Our study demonstrates that the SIP method is able to provide valuable information for the hydrogeological characterization of rock glaciers.

1 Introduction

The European Alps are undergoing drastic changes due to climate change (Beniston et al., 2018) such as retreating glaciers, the degradation of permafrost or the loss of ground ice (e.g., Biskaborn et al., 2019). The loss of ground ice has been linked to rockfalls and slope instability (e.g., Krautblatter et al., 2013; Haeberli et al., 2017) ~~; thus, poses~~ posing a threat to infrastructure and human life not only in high-mountain environments but also for downstream areas. Active rock glaciers, which consist of frozen rocks, sediments and large amounts of ground ice, move downslope resulting in surface deformation (e.g., Haeberli, 1985; Barsch, 1996). Accordingly, they can play an important role in the storage of frozen and liquid water (Jones et al., 2018; Wagner et al., 2021). Rock glaciers are more resilient towards the increase of air temperatures, compared to glaciers, as they

are protected by a top layer of large blocks and air-filled voids with low thermal conductivity (Haeberli et al., 2006; Giardino et al., 2011; Amschwand et al., 2024~~3~~). Due to the higher resilience of subsurface ice towards increasing air temperatures compared to glacier ice, future predictions expect a change in the hydrological regime in mountainous areas with a shift from glacially dominated hydrological systems to periglacially dominated systems (e.g., Haeberli et al., 2017), which has a particular impact on areas which are supplied by water from high-mountain environments (e.g., Brighenti et al., 2019).

Water, coming from snow meltwater, rainfall, groundwater, and ice meltwater, commonly percolates through intact rock glaciers as supra-permafrost flow in the active layer along the top of an ice-rich core, which is assumed to be quasi-impervious (e.g., Giardino et al., 2011; Buchli et al., 2013; Winkler et al., 2016; Krainer et al., 2007; Jones et al., 2019). The supra-permafrost flow, also called quickflow, takes place in the active layer, which is characterized by coarse-grained materials and high hydraulic conductivity (reported pore water velocity values between~~The supra-permafrost flow is also called quickflow because coarse-grained materials in the active layer are characterized by high hydraulic conductivity, with reported values in pore water velocity ranging betwee n~~ 10^{-3} and 10^{-2} m/s) (e.g., Krainer and Mostler, 2002; Buchli et al., 2013; Winkler et al., 2016; Harrington et al., 2018; Del Siro et al., 2023). Due to their high hydraulic conductivities, rock glaciers release water from heavy rainfalls quickly and they increase flood peaks when compared to catchments without rock glaciers (Geiger et al., 2014; Pourrier et al., 2014). Within rock glaciers, the ice-rich cores might be considered as quasi-impermeable as they hinder the infiltration of water from rainfalls or snowmelt. In contrast, groundwater can move underneath the frozen layer as sub-permafrost flow (also called baseflow) through fine-grained sediments (e.g., Arenson et al., 2002; Krainer et al., 2015) with lower hydraulic conductivity than the supra-permafrost layer (Winkler et al., 2016; Rogger et al., 2017). In degraded rock glaciers with only discontinuous ice layers, also rainwater and snow meltwater can percolate into deeper areas, where it accumulates leading to an increased storage capacity in the fine-grained section of the rock glacier (Pourrier et al., 2014; Winkler et al., 2016).

The monitoring of rock glacier kinematics during the last decades in the European Alps revealed an overall acceleration in the downslope movement (e.g., Delaloye et al., 2010; Wirz et al., 2014; Kellerer-Pirklbauer et al., 2024), which was first related to warming ice in rock glaciers due to increasing air temperatures (Kääb et al., 2007; Roer et al., 2008). However, recent studies demonstrate that rock glacier movement is rather dominated by the liquid water content around the shear horizon (Wirz et al., 2016; Cicoira et al., 2019). This is because most of the deformation (60-90%) occurs in the shear horizon underneath the ice-rich layer (Arenson et al., 2002; Cicoira et al., 2020), where groundwater can accumulate (Kenner et al., 2017; Buchli et al., 2018). Water accumulated within the rock glacier increases the pore water pressure and decreases the frictional resistance leading to deformation (Cicoira et al., 2019; Kenner et al., 2017). Ikeda et al. (2008) and Cicoira et al. (~~2020~~2021) demonstrated that in degrading rock glaciers water flow paths arise in thawed areas. Water from precipitation and snow melt can slowly infiltrate through such flow paths down to the shear horizon on the bottom of the rock glacier.

~~To date~~Commonly, the internal structure of rock glaciers is investigated either by boreholes or geophysical measurements. While boreholes can provide direct information about the subsurface, e.g., in terms of ice and water content, they only provide punctual~~oint-wise~~ information. Hence, borehole data need to be interpolated to resolve spatial variations in the internal

structure, which may bias the interpretation of the data, as those parameters can largely vary ~~strongly~~ in rock glaciers (e.g., Krainer et al., 2015). Moreover, core drillings in rock glaciers are ~~costly and very~~ rare (e.g., Noetzli et al., 2021), and drilling in a given position is possible only once; thus, not suited for monitoring of the ice and water content~~applications~~.

Phillips et al. (2023) installed a cross-borehole electrical resistivity tomography (ERT) monitoring on an active rock glacier. ERT is a geophysical method that allows to resolve for the variations in the electrical resistivity (ρ) of the materials (see Binley and Slater, 2021 for further details), in this case between the two boreholes. Due to the link between ρ and temperature, ERT has been used to discriminate between frozen and unfrozen materials (e.g., Kneisel et al., 2008; Mollaret et al., 2019). The ERT results can also be expressed in terms of the electrical conductivity σ (with $\sigma = 1/\rho$), which is more intuitive when used to estimate hydraulic conductivity, for instance. While initial studies assume that current can only flow through the unfrozen water filling the pores (electrolytic conductivity), quantitative interpretation of the ERT imaging results need to account for surface conductivity, which is the current flowing at the fluid-ice (or fluid-grain) interface (Stillmann et al., 2010; Maierhofer et al., 2022; 2024). The application of an external electrical field triggers not only the accumulation of charges in the electrical double layer (EDL) (surface conductivity) but also leads to a polarization effect (e.g., Vinegar and Waxman, 1984). Several studies have shown a direct relation between the surface conductivity and the polarization at low frequencies (< 10 kHz) (e.g., Revil, 2013a, Weller et al., 2013), which allows to consider the contribution of surface conductivity to the total electrical conductivity.

The induced polarization (IP) method measures both the electrical conductivity and polarization (i.e., capacitive) properties of the subsurface at low frequencies (< 10 kHz), either in the time-domain (TDIP), or in the frequency-domain (FDIP) at one single frequency (single-frequency IP) or over a broad range of frequencies (spectral IP) (for a review of the method see Binley and Slater, 2020). Recently, induced polarization has been used for an improved discrimination of ice-rich areas from bedrock (e.g., Maierhofer et al., 2022) due to the high surface charge, and in turn high polarization signature, of ice (Stillman et al., 2010).

~~To overcome the point-wise information derived from temperature sensors in boreholes, Phillips et al. (2023) installed a cross-borehole electrical resistivity tomography (ERT) monitoring on an active rock glacier. ERT is a geophysical method, which provides continuous 2D or 3D spatial information about the subsurface electrical resistivity or its inverse, the electrical conductivity; thus, it is a common tool for the detection of frozen areas because of the low electrical conductivity of ice compared to non-frozen areas (e.g., Kneisel et al., 2008; Mollaret et al., 2019). Liquid water content and electrical conductivity are directly linked as the electrical conductivity increases with increasing liquid water saturation (Archie, 1942). To quantify ice, but also air and water content, Hauck et al. (2011) proposed the so-called 4-phase model, which combines the electrical conductivity data with seismic information about the velocity of P-waves. Apart from several applications for ground ice investigations, Halla et al. (2021) used the 4-phase model to identify water pathways in an active rock glacier in the Andes and related them to surface deformation and kinematics of the rock glacier. The 4-phase model was further integrated in a joint inversion framework to estimate ice, water, air content and porosity simultaneously (Wagner et al., 2019; Mollaret et al., 2020; Steiner et al., 2021; Pavoni et al., 2023a). However, in its original formulation the model neglects variations in the surface~~

~~conductivity along the interface between grains and pore water (Waxman and Smits, 1968). When neglecting surface conductivity, the 4-phase model may overestimate the water content, as a decrease in the electrical resistivity would only be associated to an increase of interconnected pore water. Mollaret et al. (2020) applied the joint inversion framework on several different sites using different formulations of the electrical response of the four phases, one of them considered surface conductivity but only through a constant term.~~

~~The surface conductivity at low frequencies (<1 kHz) in the subsurface is due to the presence of the electrical double layer (EDL) at the grain-electrolyte interface (e.g., Waxman and Smits, 1968). During the application of an electrical field, the EDL contributes to the accumulation and polarization of charges and the development of salinity gradients that contribute to the electrical conduction. While the electrical conductivity derived from ERT consists of the electrolytic and surface conductivity, the polarization of the subsurface is only related to the surface area of particles, i.e., to the surface conductivity (Vinegar and Waxman, 1984; Revil and Florsch, 2010). As an extension of the ERT method, the induced polarization (IP) method permits to measure both the conductive and capacitive properties of the subsurface at low frequencies (< 10 kHz), either in the frequency- (FDIP) or time-domain (TDIP) (for a review of the method see Binley and Slater, 2020). Different materials with different textural properties polarize at different length-scales, which reflects in the frequency dependency of the electrical properties (see Binley et al., 2005; Revil and Florsch, 2010). For the analysis of the frequency dependence, complex conductivity measurements over a broad range of frequencies (mHz – kHz range) are necessary within the so-called spectral IP (SIP) method.~~

~~Grimm and Stillman (2015) demonstrated for the first time that field-scale resistivity measurements at different frequencies can be used to delineate areas with high ice content on the field scale. They evidenced that the so-called frequency effect (FE) in resistivity measurements, which is the relative difference between the resistivity at a high and a low frequency, increases with decreasing temperature as well as with ice content. The FE is a clear indication of induced polarization phenomena and has been used for decades in mineral exploration to delineate areas with high metal content (e.g., Seigel et al., 1959). Grimm and Stillman (2015) measured a FE of up to 0.9 between resistivity measured at 10 Hz and 19 kHz in areas with an ice content around 90% due to the polarization of ice at high frequencies (Auty and Cole, 1952; Stillman et al., 2010; Coperey et al., 2018; Limbrock et al., 2020). However, the authors did not investigate the SIP response due to unfrozen rocks and rocks with different ice content. Maierhofer et al. (2022) directly measured the polarization effect at a frequency of 75 Hz to improve the discrimination between frozen and unfrozen ground in an ice-bearing talus slope in Switzerland. Mudler et al. (2022) investigated the application of IP measurements at high frequencies (kHz range) to quantify ice content directly based on the relaxation frequency of ice (Zorin and Ageev, 2017). However~~Yet, to the best of our knowledge, no study examined the potential of SIP data for the estimation of water content and hydraulic conductivity in a rock glacier or other alpine permafrost landforms ~~yet~~.

Hydrogeological information of rock glaciers is critical to fully understand the parameters controlling their deformation and movement. Hence, the objective of this study is to understand the hydrogeological properties of the active rock glacier Gran Sometta in the Italian Alps. We evaluate the potential of SIP imaging results for the estimation of hydrogeological parameters,

namely the hydraulic conductivity and the water content. The SIP results are validated by two tracer experiments, where the distribution and flow of a saltwater injection was monitored by repeated 3D ERT images permitting the direct estimation of the pore water velocity in the rock glacier. Additionally, we investigate the link between the hydro-geophysical results and spatial variations in deformation rates of the Gran Sometta rock glacier to demonstrate the relevance of geophysical investigations to understand the main drivers of rock glacier movement in the European Alps.

~~In pharetra massa dictum gravida scelerisque. Sed vitae purus eget purus tincidunt accumsan ut at magna.~~

2 Material and Methods

2.1 Study area

The Gran Sometta rock glacier is ~~a~~ tongue-shaped ~~rock glacier~~and located in the Valtournenche valley (Aosta valley) in the Western European Alps (see Fig. 1) at an elevation between 2630 and 2770 m. The rock glacier has a total length of 400 m, a width of 150-300 m and a thickness of 20-30 m, estimated from the height of the front (Bearzot et al., 2022). At the surface, the rock glacier mainly consists of pebbles and angular blocks originating from the rock walls of the Gran Sometta peak. In the central area, longitudinal ridges dominate the structure of the morphology, while in the front part there are transversal furrows. The upper (southern) part of the rock glacier was covered by a glacier during the Little Ice Age (LIA), which still has effects on the distribution of ice content (see detailed descriptions of the rock glacier in Bearzot et al., 2022 and Bearzot et al., 2023).

The rock glacier can be split into two main lobes (see Fig. 1), which are called the white lobe (eastern part) and the black lobe (western part) as the former is mainly composed of light-colored dolomitic marbles and the latter of dark-colored carbonate-silicate schists. Apart from the color, the lobes differ in their internal structure and their kinematics (Bearzot et al., 2022). ERT results presented by Bearzot et al. (2022) revealed ~~While in the black lobe an ERT survey revealed~~ a continuous ice-rich layer with a thickness of 20 m approximately in the black lobe, while in the white lobe there are more spatial variations in the ice content, possibly related to the influence of the coverage of an LIA glacier. The rock masses in these areas possibly warmed up during the LIA due to the thermal isolation of the ice cover (Bearzot et al., 2022). Kinematic investigations of Bearzot et al. (2022) for the period 2013-2020 show that the black lobe moves faster (~1 m/y) than the white lobe (~0.5 m/y), which has been linked to the different internal structure and the steeper topography of the black lobe.

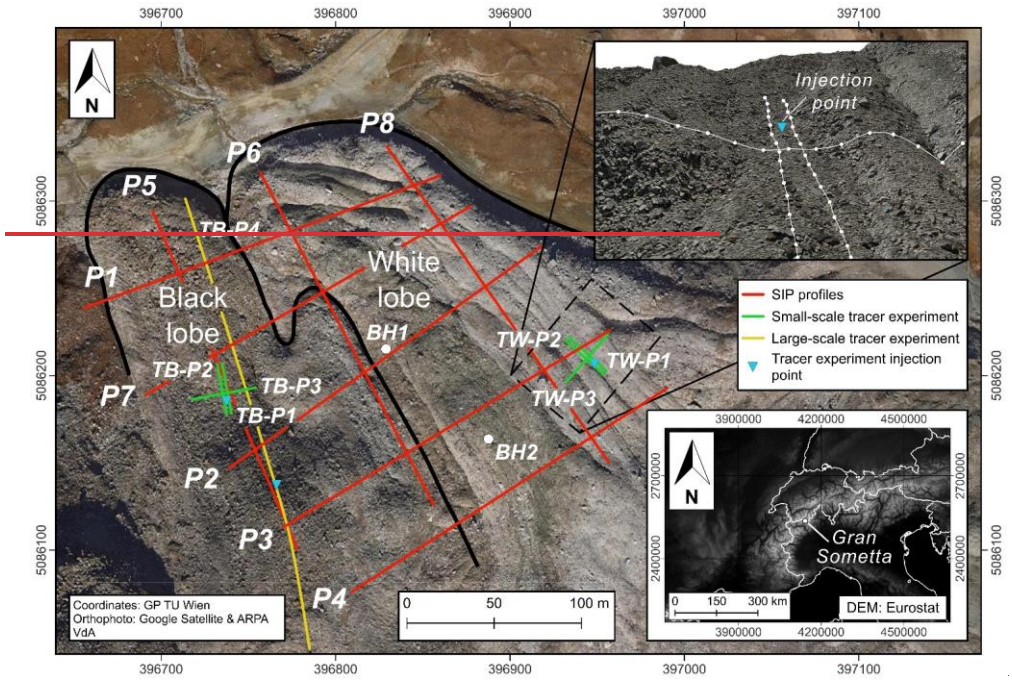
396700
396800
396900
397000
397100
N
P8
P6
P5
P1
P7
P2
P3
P4
White lobe
Black lobe
BH1
BH2
TB-P2
TB-P3
TB-P1
TW-P2
TW-P1
TW-P3
Injection point
SIP profiles
Small-scale tracer experiment
Large-scale tracer experiment
Tracer experiment injection point
Coordinates: GP TU Wien
Orthophoto: Google Satellite & ARPA VdA
0
50
100 m
5086300
5086200
5086100
3900000
4200000
4500000
2700000
2400000
Gran Sometta
0
150
300 km
DEM: Eurostat

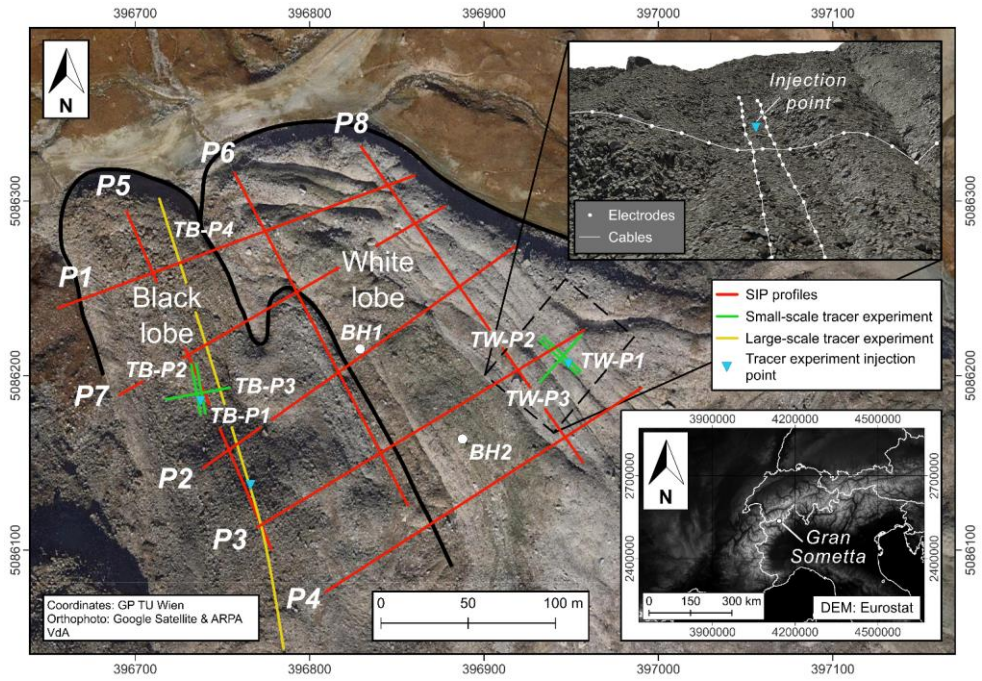

Figure 1: Map of the Gran Sometta rock glacier, which consists of two lobes, the black lobe in the west and the white lobe in the east. The SIP profiles P1-P8 are indicated by red lines, while profiles of the small-scale tracer experiments are indicated by green lines. The large-scale tracer profile is presented by a yellow line and the positions of two boreholes (BH1 and BH2) are displayed by white dots. To the ~~l~~lower right is a map of the Alps with the position of the Gran Sometta rock glacier. A 3D visualization of the area of the tracer experiment on the white lobe (TW) is given in the upper right area. Electrodes are presented by white dots, cables by white lines. Orthophoto: © Google Earth 2022; Digital Elevation model: © Copernicus.

2.2 The spectral induced polarization (SIP) method and the complex conductivity

Formatiert: Überschrift 2

IP measurements are considered as an extension of the ~~resistivity~~ ERT method and provide the conductive (electrical conductivity) and capacitive properties (polarization) of the subsurface (for an overview see Binley and Slater, 2020). When working in the frequency-domain (FDIP)~~n~~, as ~~has been done~~ in this study, an alternating current ~~,~~ at a given angular frequency ω (in the range between 1 mHz and 10 kHz) ~~with a certain angular frequency ω~~ is injected via two electrodes and the resulting

voltage is measured between two additional electrodes. The ratio between the voltage and the injected current gives a complex-valued transfer impedance $Z^*(\omega)$ consisting of a magnitude $|Z^*(\omega)|$ and a phase shift $\varphi(\omega)$ between the voltage and the current.

$$Z^*(\omega) = |Z^*(\omega)|e^{i\varphi(\omega)} \quad (1)$$

FDIP measurements can be conducted at one single frequency (single-frequency IP) or at several frequencies, which is the spectral induced polarization (SIP) method. Data at multiple frequencies~~When using the SIP method, measurements are not only conducted at one frequency, but in a broad range of frequencies, typically in the range between 1 mHz and 10 kHz to~~ provide additional information about the frequency dependence of the electrical properties~~.~~ as different materials with different textural properties polarize at different length-scales (see Binley et al., 2005; Revil and Florsch, 2010). Such information is essential for a reliable estimation of hydrogeological properties, as e.g., the hydraulic conductivity (see section 2.4).

Similar to ERT, the SIP method is based on measurements with 4 electrodes (i.e., quadrupole), where two electrodes are used for the current injection and two for conduction of measurements, yet in this case the readings are the electrical impedance. Small separation between current and potential dipole favors high resolution, while increasing their separation helps to reach deeper areas of investigation, yet at costs of decreasing the signal-to-noise ratio. At the field, combinations through tens of electrodes can be used to resolve for vertical and horizontal variations of ~~Inversion of measurements from hundreds or thousands of electrode combinations, also called quadrupoles, gives a distribution of~~ the complex-valued electrical conductivity σ^* or its inverse, the complex resistivity ρ^*.

The complex conductivity is used to represent both electrical properties of the subsurface: the electrical conduction (real part, σ') and the capacitive property (imaginary part, σ''). T~~The complex conductivity is used to represent both electrical properties of the subsurface at the low frequency: the energy conduction (presented in the real component σ') and the energy stored due to the polarization of charges accumulated at the EDL (imaginary component σ''). T~~he σ^* can also be represented by its magnitude $|\sigma^*|$ and phase angle $\varphi(\omega)$:

$$\sigma^*(\omega) = \sigma'(\omega) + i\sigma''(\omega) = |\sigma^*(\omega)|e^{i\varphi(\omega)} \quad (2)$$

In areas free of metallic materials $|\sigma^*|$ is approximately equal to σ' because $\varphi(\omega)$ is relatively low (typically below 100 mrad) (~~Binley and Slater, 2020~~Kemna et al., 2004).

~~Current can be conducted through the subsurface by via three different mechanisms~~: matrix conductivity, electrolytic conductivity and surface conductivity (see Eq. (3))~~:~~. (1) ~~(1)~~ The matrix conductivity σ_m ~~describes~~ refers to the current conduction through the solid (i.e., grains and matrix). This mechanism is negligible at sites without electronic conductors and semi-conductors like metallic minerals, such as in rock glaciers. (2) The electrolytic conductivity σ_{el} (Eq. (4)) ~~describes~~ is conduction~~current conduction~~ through the pore fluid. It is dominated by ~~, which depends on~~ the porosity ϕ, the cementation exponent m (which can be also expressed by the formation factor $F = \phi^{-m}$), the saturation S_w, the saturation exponent n and the fluid conductivity σ_f (see e.g., Archie, 1942). (3) The surface conductivity ~~σ_s^* describes the conduction, represented by the real part σ_s', and the polarization, represented by the imaginary part σ_s'',~~ takes place in the ~~electric double layer (~~EDL~~)~~ at the

interface between solid particles and the pore fluid. This conduction mechanism ~~σ_s^*~~ is ~~dominated~~controlled by the surface area and surface charge of particles and is frequency dependent (e.g., Waxman and Smits, 1968).

$$\sigma'(\omega) = \sigma_m + \sigma_{el} + \sigma_s'(\omega) \quad (3)$$

$$\sigma_{el} = S_w^n F^{-1} \sigma_f \quad (4)$$

The imaginary component of the complex conductivity is only dependent on the imaginary component of the surface conductivity because the pore water is assumed to be non-polarizable at frequencies below 10 kHz:

$$\sigma''(\omega) = \sigma_s''(\omega) \quad (5)$$

In the absence of electronically conductive materials, the polarization is ~~only~~ primarily related to the surface area and the surface charge of the particles (Vinegar and Waxman, 1984; Leroy et al., 2008; Revil and Florsch, 2010).

2.3 SIP field measurements, data processing and inversion

Formatiert: Überschrift 2

In October 2022, we collected SIP data along eight lines (P1 to P8) on the Gran Sometta rock glacier (see Table 1). P5, P6 and P8 are longitudinal lines and P1, P2, P3, P4 and P7 are transversal to the flow direction of the rock glacier (see Fig. 1). Different line orientations allow to collect data of quadrupoles with different dipole orientations, which provides a good coverage of the subsurface electrical properties in all directions (see e.g., Chambers et al., 2002; Moser et al., 2023). For each line of electrodes, we used 32 stainless-steel electrodes with a separation of 7.5 m. We collected data using dipole-dipole (DD) normal and DD reciprocal (electrodes used for current and voltage dipole interchanged) configurations for analysis of data error (see e.g., LaBrecque et al., 1996). We also collected data using a multiple-gradient (MG) configuration which are related to higher signal-to-noise ratio (S/N) than DD. While DD data was collected with a dipole length of four times the electrode spacing (i.e., skip-3), MG readings were used with voltage dipole using a skip-0, skip-1, skip-2 and skip-3 configuration, and the current dipoles wrapping the eight potential dipoles. Due to the lower number of independent current injections, with the MG configuration we collected data in a frequency range of 0.1-225 Hz, with the DD configuration we used a frequency range of 0.5-225 Hz due to time-constraints on the field. For the data acquisition, we used the eight-channel device DAS-1 (Data Acquisition System, from MPT-IRIS Inc.), which was connected to stainless steel electrodes via coaxial cables (COAX10, designed at TU Wien; see Flores Orozco et al., 2021). The isolation of coaxial cables permits to avoid electromagnetic (EM) coupling due to cross-talk between the cables as demonstrated by Flores Orozco et al. (2013 and 2021), and (in alpine permafrost) by Maierhofer et al. (2022).

The SIP data were processed in four steps: (1) We calculated the geometric factors k_{num} as the ratio between numerically modeled transfer resistances of a homogeneous synthetic model and the resistivity of the homogeneous model. Readings with an inconsistent polarity between k_{num} and the measured transfer resistances were deleted as erroneous readings. (2) All readings with an absolute misfit between normal and reciprocal above two times the standard deviation of the normal-reciprocal misfit for the entire data set, as well as those readings with a relative normal-reciprocal misfit (above 5% in the case of $|Z^*|$, and 50% in the case of φ) were removed, similar to the filtering protocol of Flores Orozco et al. (2019). (3) Additionally,

outliers in the readings of apparent resistivity $|\rho_a^*|$, defined as those below 10^3 Ωm and above 10^5 Ωm, as well as positive impedance phase values (φ) were removed. The apparent resistivity thresholds were defined based on a histogram analysis, where large gaps at the margin of the data distribution were identified as thresholds, resulting in approximately 5-6 removed quadrupoles per electrode line. Steps 1 to 3 were conducted separately for each frequency. (4) Similar to Moser et al. (2023), readings, which were removed during steps 1 to 3 in at least one frequency, were removed in all frequencies to keep the same quadrupoles for the inversion of data collected at all frequencies, aiming at having consistent sensitivity in the inverted images (Flores Orozco et al., 2013). After applying filtering steps (1) – (4) 731 of 1792 quadrupoles remained in the case of the MG configuration and 359 of 4416 in the case of the DD configuration. Considering the high density of measurements collected with the MG configuration designed in our study, the number of filtered measurements has just a minimal effect on the coverage and resolution of our data sets, as demonstrated, for instance, in the pseudosection (in terms of $|\rho_a^*|$) presented in the Appendix (see Fig. A1). From now on, for all multi-frequency analyses, we only consider MG data because of the larger range of frequencies used for the data collection with the MG configuration (0.1-225 Hz) than with the DD configuration (0.5-225 Hz).

We inverted the data collected at each frequency independently using the ResIPy code (Blanchy et al., 2020), which calls the cR3t 3D complex resistivity inversion algorithm (for details see Binley and Slater, 2020). cR3t is a smoothness-constrained algorithm based on complex calculus, which iteratively solves for a 3D complex conductivity model. The 3D model is represented by a finite element mesh, which is created in Gmsh (Geuzaine and Remacle, 2009). The mesh is based on tetrahedral elements, whose sizes increase with increasing distance from the electrodes, and it incorporates the topography by a digital terrain model.

The inversion algorithm fits the data under the consideration of an error model to a certain level of confidence (Binley and Kemna, 2005), which is here represented by the error-weighted root-mean square error (RMS) between the data and the forward solution of the inverse model. The error model consists of a relative magnitude error, which for our measurements was estimated at 10%, as well as an absolute phase error, which in our measurements was estimated at 7 mrad (at 0.1 Hz) and increased to 43 mrad (at 25 Hz) due to the increasing contamination of EM coupling with increasing frequency in the data (e.g., Binley et al., 2005). All inversions converged and resulted in an error-weighted RMS value equal or close to 1.

	Profile	Date	Number of electrodes	Electrode separation (m)	Configuration	Number of quadrupoles	Frequency (Hz) / Pulse length (ms)	Number of repetitions
Mapping	P1-P8	October 13th-17th 2022	32 per profile	7.5	DD, MG	552 (DD), 224 (MG) per profile	0.5-225 Hz (DD), 0.1-225 Hz (MG)	0
Trace	TW-P1, TW-P2, TW-P3	October 19th 2022	16 (P1), 16 (P2), 20 (P3)	2	DD	498	7 Hz	91

Formatierte Tabelle

Formatiert: Einzug: Links: 0.2 cm, Rechts: 0.2 cm

hat formatiert: Hochgestellt

hat formatiert: Hochgestellt

Formatiert: Einzug: Links: 0.2 cm, Rechts: 0.2 cm

hat formatiert: Hochgestellt

TB-P1, TB-P2, TB-P3	August 22nd 2023	16 (P1), 16 (P2), 20 (P3)	2	DD	498	7 Hz	70
TB-P4	August 23rd 2023	72	5	DD	4032	250 ms	16

Table 1: Overview of electrical measurements.

hat formatiert: Hochgestellt

hat formatiert: Hochgestellt

2.43 Deriving hydraulic conductivity from SIP measurements

The IP polarization (capacitive property)method provides information about textural properties of the subsurface, which control the ability of water to flow, i.e., its hydraulic properties (see Binley and Slater; 2020). According to the Kozeny-Carman equation, geometric parameters, i.e., the hydraulic radius and the tortuosity, are dominating the hydraulic conductivity of the subsurface (Carman, 1939; Kozeny, 1927). These parameters can be derived from IP and SIP measurements as the tortuosity is linked to the electrolytic conductivity and the hydraulic radius is related to the surface conductivity (for a review see Slater, 2007). Using only electrical conductivity and neglecting surface conductivity in the estimation of hydraulic conductivity can bears the risk of over-estimating the hydraulic properties, as the contribution to current conduction through the EDL is incorrectly assumed to be through a higher porosity and charge transfer across the electrolyte filling the pores.lead to an ambiguity On the one hand, as in the case of relatively coarse-grained materials, e.g.,such as sands and gravels, the electrolytic conductivity dominates over the surface conductivity. In such media the hydraulic conductivity increases with increasing porosity, which in turn increases the electrolytic conductivity, resulting in a positive correlation between electrical and hydraulic conductivity (e.g., Frohlich et al., 1996). On the other hand, If the materials arein relatively fine-grained materials (clays and fine silts), the surface conductivity dominates over the electrolytic conductivity. In such media the hydraulic conductivity decreases with increasing clay content as the pores are less connected hindering water flow, which in turn increases the surface conductivity leading resulting in a negative correlation between electrical and hydraulic conductivityto an opposite correlation because the pores are less connected hindering water flow (e.g., Urish et al., 1981). Accounting for surface conductivity through the use of IP measurements improves hydraulic conductivity estimations, as demonstrated in the laboratory (e.g., Binley et al., 2005; Revil and Florsch, 2010; Slater et al., 2014; Weller et al., 2015) and on the field scale (e.g., Hördt et al. 2009; Benoit et al., 2019; Soueid Ahmed et al., 2020; Kemna et al., 2004).

Several studies have demonstrated an improvement of the hydraulic conductivity estimation when considering the frequency dependence of the polarization, because the frequency dependence is particularly linked to different length scales of the pore space (e.g., Binley et al., 2005; Revil et al., 2015). Thus, SIP measurements permit an improved estimation of the hydraulic properties, as observed from laboratory (e.g., Revil and Florsch, 2010; Slater et al., 2014; Weller et al., 2014; Weller et al., 2015) and field scale investigations (e.g., Hördt et al. 2009; Benoit et al., 2019; Flores Orozco et al., 2022). However, investigations in different environments demonstrate that there is no universal model linking SIP parameters and hydraulic conductivity, thus, every model applied on the field needs to be carefully evaluated (see Slater, 2007).

2.4-5 The relation between complex conductivity and hydrogeological parameters

The volumetric water content θ of porous media is directly linked to the electrical conductivity σ' via F, S_w and n (see Eq. (4)), which allows to estimate θ based on σ'. However, as described above, σ' is not only related to σ_{el} but also to σ'_s (see Eq. (3)). To take σ'_s into account, in this study we use the dynamic stern layer model DSLM (Revil, 2013a,b), which provides the following equations for the instantaneous (high frequency) conductivity σ_∞ and the direct current (low frequency) conductivity σ_0, where the first term represents the frequency independent σ_{el} and the second term the frequency dependent σ'_s:

$$\sigma_\infty = \theta^m \sigma_f + \theta^{m-1} \rho_g B \, CEC \quad (6)$$

$$\sigma_0 = \theta^m \sigma_f + \theta^{m-1} \rho_g (B - \lambda) \, CEC, \quad (7)$$

where ρ_g is the grain density (kg m^{-3}), B is the apparent mobility of the counterions for surface conduction (m^2 s^{-1} V^{-1}) and λ is the apparent mobility of the counterions for the polarization (m^2 s^{-1} V^{-1}). CEC is the cation exchange capacity (C kg^{-1}), which is directly linked with the clay content (Mao et al., 2016) and the normalized chargeability M_n, which is the difference between σ_∞ and σ_0, but can also be calculated by the difference between the conductivity at a high frequency f_2 and the conductivity at a low frequency f_1.

$$M_n = \sigma_\infty - \sigma_0 = \theta^{m-1} \rho_g \lambda \, CEC \quad (8)$$

In the case of a broad distribution of grain sizes, the spectrum of the conductivity phase angle is rather flat and can be roughly described by a constant phase angle model, the so-called Drake's model (Van Voorhis et al., 1973). If such model is applicable, M_n is linearly related to σ'' (at the geometric mean frequency between f_1 and f_2) by the factor α, as demonstrated by laboratory and field investigations (see Revil et al., 2017; Revil et al., 2021):

$$\sigma'' = -\frac{M_n}{\alpha} \quad (9)$$

$$\alpha = \frac{2}{\pi} \ln(A), \quad (10)$$

where A is the number of decades between f_1 and f_2.

(Revil et al., 2017):

$$A = \log_{10}\left(\frac{f_2}{f_1}\right). \quad (11)$$

We used the difference between the conductivity real part at 25 Hz and 0.1 Hz of the MG inverse model for the calculation of M_n as proposed by Revil et al. (2021). In contrast to Revil et al. (2021), the linear relation between M_n and σ'' is weak (see Fig. 2c) with a large contrast between the predicted and the estimated slope α (10.11 and 3.37). This discrepancy is due to the strong increase of φ and the non-linear increase of $|\sigma^*|$ at frequencies above 2.5 Hz as presented in Fig. 2a (here marked as 'High frequency range'), and therefore does not fulfill the conditions of the DSLM. Above 2.5 Hz, the surface conductivity is not only controlled by the accumulation and polarization of charges within the EDL at the grain-fluid interface, but also at the ice-water interface as observed by Stillman et al. (2010). The contribution of ice to the polarization at high frequencies is not considered in the DSLM (Coperey et al., 2019); thus, we decided to calculate M_n based on the conductivity resolved at 0.1

hat formatiert: Nicht Hervorheben

hat formatiert: Nicht Hervorheben

hat formatiert: Nicht Hervorheben

hat formatiert: Nicht Hervorheben

and 2.5 Hz (in Fig. 2a marked as 'Low frequency range'). As presented in Fig. 2b, such analysis results in a stronger correlation between M_n and σ'' with similar predicted and estimated values for α (2.06 and 1.91).

~~To estimate water content θ and hydraulic conductivity K based on the DSLM in the Gran Sometta rock glacier, we calculated M_n as the difference between the conductivity real part at 25 Hz and 0.1 Hz of the MG inverse model using equation 8 proposed in Revil et al. (2020). However, this equation is only valid in the case of a constant phase angle and a linear relation between M_n and σ''. In our case, the linear relation between M_n and σ'' is weak (see Fig. 3c) with a large contrast between the predicted and the estimated slope α (10.11 and 3.37). Such discrepancy is due to the strong increase of φ and the non-linear increase of $|\sigma^*|$ at frequencies above 2.5 Hz as presented in Fig. 3a (here marked as 'High frequency range'). Above 2.5 Hz, the surface conductivity is not only controlled by the accumulation and polarization of charges within the EDL at the grain-fluid interface, but also at the ice-water interface as observed by Stillman et al. (2010). The contribution of ice to the polarization at high frequencies is not considered in the DSLM (Coperey et al., 2019); thus, we decided to calculate M_n based on the conductivity resolved at 0.1 and 2.5 Hz (in Fig. 3a marked as 'Low frequency range'). As presented in Fig. 3b, such analysis results in a stronger correlation between M_n and σ'' with similar predicted and estimated values for α (2.06 and 1.91). However, the smaller the frequency window for the calculation of M_n is, the higher is the probability of overlooking polarization effects at higher frequencies, apart from ice polarization.~~

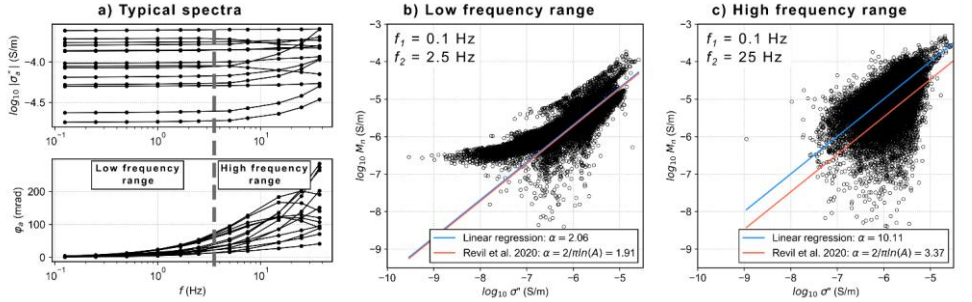

Figure 2: a) Typical spectra of the apparent conductivity magnitude and phase shift of the Gran Sometta rock glacier. b) and c) present the relation between the normalized chargeability, calculated from a low frequency f_1 and a high frequency f_2, and the imaginary part of the complex conductivity at the geometric mean frequency between f_1 and f_2, for the low (b) and high frequency range (c). The blue line indicates a linear regression, while the red line represents the theoretical relation (Revil et al., 2020). The data shown here were collected with a MG configuration along P1-P8.

If we combine equations 6 and 8, we can formulate expressions for θ and CEC (Revil et al., 2020):

$$\theta = \left[\frac{1}{\sigma_f}\left(\sigma_\infty - \frac{M_n}{R}\right)\right]^{1/m} \quad (12\text{~~1~~})$$

$$CEC = \frac{M_n}{\theta^{m-1}\rho_g\lambda} \quad (13\text{~~2~~})$$

hat formatiert: Nicht Hervorheben
hat formatiert: Nicht Hervorheben
hat formatiert: Nicht Hervorheben
hat formatiert: Nicht Hervorheben
hat formatiert: Nicht Hervorheben
hat formatiert: Nicht Hervorheben
hat formatiert: Nicht Hervorheben
hat formatiert: Nicht Hervorheben
hat formatiert: Schriftart: Englisch (Vereinigtes Königreich)
hat formatiert: Nicht Hervorheben
hat formatiert: Schriftart: Fett

where R is the ratio between λ and B. Laboratory investigations have shown that R is a dimensionless constant value in a range of 0.1±0.02 (Revil et al., 2017a,b,c). To determine σ_f for equation 1~~1~~2, we measured σ_f at the spring of the white and black lobe, which is in a range of 0.02-0.03 S/m. ~~The~~ The water stored within the rock glacier increases its σ_f over time because of its contact with subsurface materials, like rocks and sediments. Therefore, the σ_f of the water stored in the rock glacier is lower than the water released at the rock glacier springs. To take into account the increase in the fluid conductivity of the water stored in the rock glacier over time, we used a value of 0.01 S/m. ~~To take into account the increase in the salinity of the water stored in the rock glacier in contact with rock material, we used a value of 0.01 S/m, as the measured fluid conductivities represent the value measured at the rock glacier spring at its maximum.~~ For m we used 2, as used by Coperey et al. (2019), and for ρ_g we used the mean grain density of green schist, dolomite and marble (2700 kg m^{-3}).

Soueid Ahmed et al. (2020) further developed the DSLM for the estimation of the permeability k (m^2) in unsaturated media based on θ, CEC and the fitting parameter k_0.

$$k \approx \frac{k_0 \theta^6}{(\rho_g CEC)^2} \quad (1\text{~~1~~}3)$$

θ and CEC were calculated by equations ~~11~~ 12 and ~~12~~13, for k_0 we used a value of $10^{4.3}$ as estimated in the laboratory by Soueid Ahmed et al. (2020). In a next step, we converted k into the hydraulic conductivity K (m/s) by the following equation:

$$K = \frac{g\delta}{\mu} k \quad (1\text{~~5~~}4)$$

where we used reference values for the gravitational acceleration g ($g = 9.81$ m s^{-2}) and for the groundwater dynamic viscosity μ ($\mu = 1.0 \times 10^{-3}$ kg m^{-1} s^{-1}). For the density of the fluid δ, we assumed 1000 kg m^{-3}. K can be converted into the pore water velocity v_p under the consideration of the porosity ϕ, where we used a mean value of 40% (as used as an approximate value in other rock glacier studies, e.g., Hauck et al., 2011; Halla et al., 2021) and the hydraulic gradient $\frac{\Delta H}{\Delta L}$. The hydraulic gradient is the ratio between the difference in height ΔH and the horizontal distance ΔL between two points and which we estimated from a digital elevation model:

$$v_p = \frac{K}{\phi} \frac{\Delta H}{\Delta L} \quad (1\text{~~6~~}5)$$

~~To estimate water content θ and hydraulic conductivity K based on the DSLM in the Gran Sometta rock glacier, we calculated M_π as the difference between the conductivity real part at 25 Hz and 0.1 Hz of the MG inverse model using equation 8 proposed in Revil et al. (2020). However, this equation is only valid in the case of a constant phase angle and a linear relation between M_π and σ''. In our case, the linear relation between M_π and σ'' is weak (see Fig. 3c) with a large contrast between the predicted and the estimated slope α (10.11 and 3.37). Such discrepancy is due to the strong increase of ϕ and the non-linear increase of $|\sigma^*|$ at frequencies above 2.5 Hz as presented in Fig. 3a (here marked as 'High frequency range'). Above 2.5 Hz, the surface conductivity is not only controlled by the accumulation and polarization of charges within the EDL at the grain–fluid interface, but also at the ice–water interface as observed by Stillman et al. (2010). The contribution of ice to the polarization at high~~

hat formatiert: Nicht Hervorheben

frequencies is not considered in the DSLM (Coperey et al., 2019); thus, we decided to calculate M_{π} based on the conductivity resolved at 0.1 and 2.5 Hz (in Fig. 3a marked as 'Low-frequency range'). As presented in Fig. 3b, such analysis results in a stronger correlation between M_{π} and σ'' with similar predicted and estimated values for α (2.06 and 1.91). However, the smaller the frequency window for the calculation of M_{π} is, the higher is the probability of overlooking polarization effects at higher frequencies, apart from ice polarization.

2.5 SIP field measurements and data processing

In October 2022, we collected SIP data along eight lines (P1 to P8) on the Gran Sometta rock glacier. P5, P6 and P8 are longitudinal lines and P1, P2, P3, P4 and P7 are transversal to the flow direction of the rock glacier (see Fig. 1). Different line directions allow to collect data of quadrupoles with different dipole orientations, which provides a good coverage of the subsurface electrical properties in all directions (see e.g., Chambers et al., 2002; Moser et al., 2023). For each line of electrodes, we used 32 stainless-steel electrodes with a separation of 7.5 m. We used two configurations: a dipole-dipole (DD) normal and reciprocal (current and voltage dipole changed) configuration (see e.g., LaBrecque et al., 1996) with a dipole length of four times the electrode spacing, and a multiple-gradient (MG) configuration. With the DD configuration, we collected data in a frequency range of 0.5-225 Hz, with the MG configuration we used a frequency range of 0.1-225 Hz. For the data acquisition, we used the eight-channel device DAS-1 (Data Acquisition System, from MPT-IRIS Inc.), which was connected to stainless steel electrodes via coaxial cables (COAX10, designed at TU Wien; see Flores Orozco et al., 2021). The isolation of coaxial cables permits to avoid electromagnetic (EM) coupling due to cross-talk between the cables as demonstrated by Flores Orozco et al. (2013 and 2021), and (in alpine permafrost) by Maierhofer et al. (2022).

The SIP data were processed in four steps: (1) We calculated the geometric factors k_{num} as the ratio between numerically modeled transfer resistances of a homogeneous synthetic model and the resistivity of the homogeneous model. Readings with an inconsistent polarity between k_{num} and the measured transfer resistances were deleted as erroneous readings. (2) All readings with an absolute misfit between normal and reciprocal above two times the standard deviation of the normal-reciprocal misfit for the entire data set, as well as those readings with a relative normal-reciprocal misfit (above 5% in the case of $|Z^*|$, and 50% in the case of φ) were removed, similar to the filtering protocol of Flores Orozco et al. (2019). (3) Additionally, outliers in the readings of apparent resistivity $|\rho_a^*|$, defined as those below 10^3 Ωm and above 10^5 Ωm, as well as positive impedance phase values (φ) were removed. Steps 1 to 3 were conducted separately for each frequency. (4) Equal to the routine of Moser et al. (2023), readings, which were removed during steps 1 to 3 in at least one frequency, were removed in all frequencies to keep the same quadrupoles for the inversion of data collected at all frequencies, aiming at having consistent sensitivity in the inverted images (Flores Orozco et al., 2013). After applying filtering steps (1) – (4) 731 of 1792 quadrupoles remained in the case of the MG configuration and 359 of 4416 in the case of the DD configuration. Considering the high density of measurements collected with the MG configuration designed in our study, the number of filtered measurements has just a minimal effect on the coverage and resolution of our data sets, as demonstrated, for instance, in the pseudosection (in terms of $|\rho_a^*|$) presented in the Appendix (see Fig. A1). From now on, for all multi-frequency analyses, we only consider MG

Kommentiert [CM1]: PART 2

~~data because of the larger range of frequencies used for the data collection with the MG configuration (0.1-225 Hz) than with the DD configuration (0.5-225 Hz).~~

~~We inverted the data collected at each frequency independently using the ResIPy code (Blanchy et al., 2020), which calls the cR3t 3D complex resistivity inversion algorithm (for details see Binley and Slater, 2020). cR3t is a smoothness-constrained algorithm based on complex calculus, which iteratively solves for a 3D complex conductivity model. The 3D model is represented by a finite element mesh, which was created in Gmsh (Geuzaine and Remacle, 2009). The mesh is based on tetrahedral elements, whose sizes increase with increasing distance from the electrodes, and it incorporates the topography by a digital terrain model. The inversion algorithm fits the data under the consideration of an error model to a certain level of confidence (Binley and Kemna, 2005), which is here represented by the error-weighted root-mean square error (RMS) between the data and the forward solution of the inverse model. The error model consists of a relative magnitude error, which for our measurements was estimated at 10%, as well as an absolute phase error, which in our measurements was estimated at 7 mrad (at 0.1 Hz) and increased to 43 mrad (at 25 Hz) due to the increasing contamination of EM coupling with increasing frequency in the data (e.g., Binley et al., 2005). All inversions converged and resulted in an error-weighted RMS value equal or close to 1.~~

2.~~6~~ 7 Resistivity tracer experiment

Several studies have demonstrated the value of monitoring saltwater tracer tests by time-lapse ERT to investigate hydraulic connections between different geological units or to directly estimate hydraulic conductivity of the subsurface (e.g., Kemna et al., 2002; Singha and Gorelick, 2005; Cassiani et al., 2006; Perri et al., 2012) because the electrical conductivity is sensitive to saltwater due to its high fluid conductivity. ~~Commonly, the dispersion of a tracer is monitored through chemical analyses of samples from several sampling points, e.g., boreholes. However, such information gives only discrete information about the tracer flow and can fail if the tracer escapes from the sampling points (Cassiani et al., 2006). Coupling tracer experiments with time-lapse ERT monitoring overcomes such limitation as the method provides continuous images of the subsurface over time, which can be used to describe the movement and the dispersion of the fluid (e.g., Camporese et al., 2011).~~

We carried out three water amendments into the subsurface, two small and one large tracer tests, identified in such way by the volume of water injected, and the geometry of the ERT arrays for monitoring. One of the small tracer tests was conducted in the white lobe (TW) in October 2022 and the second one in the black lobe (TB) in August 2023 (see Table 1, and location in Fig. 1). The small tracer tests aimed at investigating the dispersion properties of water in the rock glacier, particularly to estimate the hydraulic conductivity in the active layer. For each small tracer experiment, we injected 70 l of saltwater in 4.5 minutes (29 g NaCl per liter; $\sigma_f = 41.5$ mS/cm at the white lobe and $\sigma_f = 51.5$ mS/cm at the black lobe; the discrepancy in σ_f is most likely related to the difference in the water temperature (10°C and 19°C)) ~~in 4.5 minutes.~~ We~~and~~ conducted resistivity measurements (498 quadrupoles) every 2 minutes and 10 seconds along three lines for 3 hours and 20 minutes (see Fig. 1) in the frequency-domain at 7 Hz with a stacking of 2 (see Table 1). We decided upon 7 Hz instead of a lower frequency to decrease the measurement time; thus, increasing the temporal resolution of the ERT monitoring. Test measurements at 7 Hz

(data not shown) showed similar data quality compared to lower frequencies (1 Hz). The ERT setup consists of two parallel lines per lobe (profile TW-P1 and TW-P2, and TB-P1 and TB-P2 respectively), which are longitudinal to the rock glacier flow direction and include 16 electrodes per line, and one transversal profile per lobe (TW-P3 and TB-P3) consisting of 20 electrodes, which crosses TW-P1 and TW-P2, and TB-P1 and TB-P2 respectively, 4 m away from the injection point (see Fig. 1). For all time steps, we used a DD skip-1 protocol with inline (current and voltage dipole in one line) and crossline (current and voltage dipole in two different lines) quadrupoles along TW-P1 and TW-P2, and TB-P1 and TB-P2 respectively, and DD skip-1 inline measurements along TW-P3 and TB-P3 respectively. ~~The number of skips is the number of electrodes skipped within a dipole.~~ One full SIP measurement (0.5-225 Hz) was conducted before the start of the tracer injection and the 7 Hz data were used as the baseline dataset (time step 0) for the ERT monitoring. After 24 minutes, we repeated the tracer experiment with the same protocol to validate the results of injection 1.

The large tracer experiment aimed at investigating larger paths for water conduction and was ~~conducted~~ performed in August 2023. To this end, we injected 425 l saltwater ($\sigma_f = 51.5$ mS/m) over 6 minutes on the black lobe (see Fig. 1). We repeated ERT measurements every 15 minutes along a 355 m long 2D profile (TB-P4 in Fig. 1) with an electrode separation of 5 m. ERT measurements were carried out with a DD schedule in the time-domain with a pulse length of 250 ms. Apart from the ERT monitoring, we measured the fluid conductivity (1 minute sampling interval) at the rock glacier springs in the front over three days during the tracer tests in the black lobe, but we did not identify any changes related to the arrival of the tracer. The application of discrete sampling methods within the boreholes was impossible because the boreholes are used for temperature monitoring and are not suited for the extraction of water samples.

In the processing of the ERT data collected during the tracer tests, we removed measurements with a wrong polarity in all time steps and kept only those quadrupoles, which were found in all time steps to invert for imaging results with similar sensitivity, analogously to the step followed for the comparison of inversion results for different frequencies in the SIP data. For the small-scale tracer experiments, we inverted the time-lapse data of the two parallel electrode lines (TW-P1 and TW-P2; TB-P1 and TB-P2 respectively) three-dimensionally in ResIPy (Blanchy et al., 2020), with a time-lapse background constrained inversion (TLBC) under the consideration of a relative error of 10%. We used the TLBC approach because the comparison with results of a time-lapse difference approach (TLD) and the independent (IDP) inversion of all time steps showed that in areas where we expected no changes over time, we revealed less changes in the resistivity images of the TLBC approach than in the images of the IDP and TLD inversion (data not shown here). Data collected along the profiles perpendicular to the parallel lines (TW-P3 in the white lobe and TB-P3 in the black lobe) were not considered in the inversion as we did not observe any saltwater movement perpendicular to the elevation gradient (data not shown here). For the large-scale tracer experiment, we also decided upon the TLBC inversion approach as we observed smoother changes in the conductivity over time than with the IDP and TLD approach.

2.~~7~~ 8 Kinematic analysis to evaluate surface deformation

The surface of the Gran Sometta rock glacier is regularly monitored by UAV surveys. They are carried out every year at the end of August to produce an orthomosaic and a digital surface model (DSM) of the rock glacier, which is used to understand surface deformation (results from the period 2016-2019 were published in Bearzot et al., 2022). Technical details about the UAV campaigns can be found in Table ~~1~~2. The images collected are processed using a Structure-from-Motion (SfM) workflow implemented in the commercial software Agisoft Metashape. A network of 23 painted targets was used as ground control points (12) and check points (11). The RMSE value for each survey is shown in Table 2~~1~~ (XY error). The horizontal displacements were calculated for the periods 2020-2023 and 2022-2023 using the positions of blocks detected through photointerpretation on orthomosaics with a resolution of 2 cm/pixel. The spatial distribution of the rock features was defined using a square grid of 20 x 20 m. The position of the most representative targets for each year was defined manually and the horizontal displacement of the chosen points was calculated using the Qgis plugin "PointsToPaths".

Date	Covered area (km^2)	Ground sampling distance (cm/px)	UAV model	Camera model	Number of images	Mean flying altitude (m AGL)	XY error (cm) - check points RMSE
August 21st 2020	0.337	2.33	DJI Phantom 4 Pro V2	FC6310 (lens 35 mm)	665	85	1.82
August 20th 2022	0.36	1.35	DJI M300 RTK	Zenmuse DJI P1 (lens 35 mm)	763	115	3.20
August 21st 2023	0.36	1.39	DJI M300 RTK	Zenmuse DJI P1 (lens 35 mm)	790	120	1.50

Table ~~1~~2: Technical details of the UAV surveys.

3 Results

3.1 Electrical properties of the Gran Sometta rock glacier

The 3D inverse model of data collected with a MG and DD configuration at 0.5 Hz is shown in Fig. 2~~3~~. The inversion results are presented in terms of the ~~in-phase component~~conductivity real part σ', the ~~quadrature component~~conductivity imaginary part σ'' and the phase φ of the complex conductivity, and visualized by slices cut through the 3D model vertically along the electrode lines. Along the longitudinal profiles P8 (white lobe) and P5 (black lobe) we can identify three main layers: The top layer is, in comparison to the generally highly resistive media in mountain permafrost, conductive ($\sigma' >$ ~~$10^{-4.25}$~~56 µS/m; or by

its inverse, the resistivity ρ < 17857~~$10^{4.25}$~~ Ωm) and polarizable (σ'' > ~~$10^{-6.5}$~~0.3 µS/m) with a thickness of 4-6 m. ~~top layer is related to unfrozen sediments and rocks in the active layer with a thickness of approximately 4-6 m, in this case associated to blocky but also fine-grained materials (Bearzot et al., 2022). No direct validation data of active layer thickness for the measurements in 2022 and 2023 is available because boreholes with temperature sensors in the Gran Sometta rock glacier were destroyed in 2018. However, the active layer thickness estimation is in a similar range as the value determined from the boreholes (6 m in borehole 1 and 4 m in borehole 2) during 2015-2016 (see Fig. A2). We expect an active layer thickness in 2022 still in a range between 4 and 6 m as rock glaciers are more resilient towards increasing air temperatures compared to other permafrost features (e.g., Pruessner et al., 2021).~~ The second layer along the white and the black lobe is 20-30 m thick, ~~is~~ resistive (σ' < ~~$10^{-4.25}$~~56 µS/m, i.e., with a resistivity ρ > 17857 ~~$10^{4.25}$~~ Ωm) and less polarizable (σ'' < ~~$10^{-6.5}$~~0.3 µS/m). Below this resistive and less polarizable layer, there are again materials with relatively high σ'_{AA} and σ''_{A}. While the electrical properties along P5 and P8 are horizontally layered with a relatively continuous resistive and polarizable layer, we can observe higher spatial variability in the center of the rock glacier, at the position where both the white and the black lobe intersect. Such area is covered by all profiles apart from P5 and P8 and can be characterized by maximum values in σ' and σ'' in all layers. ~~corresponding to the frozen materials with a thickness of 20-30 m, in agreement with results from Bearzot et al. (2022). The bottom layer corresponds to the unfrozen materials related to higher electrical conductivity and polarization values (i.e., σ' and σ'').~~

hat formatiert: Nicht Hervorheben

hat formatiert: Nicht Hervorheben

hat formatiert: Nicht Hervorheben

hat formatiert: Nicht Hervorheben

hat formatiert: Nicht Hervorheben

Kommentiert [CM2]: PART 1

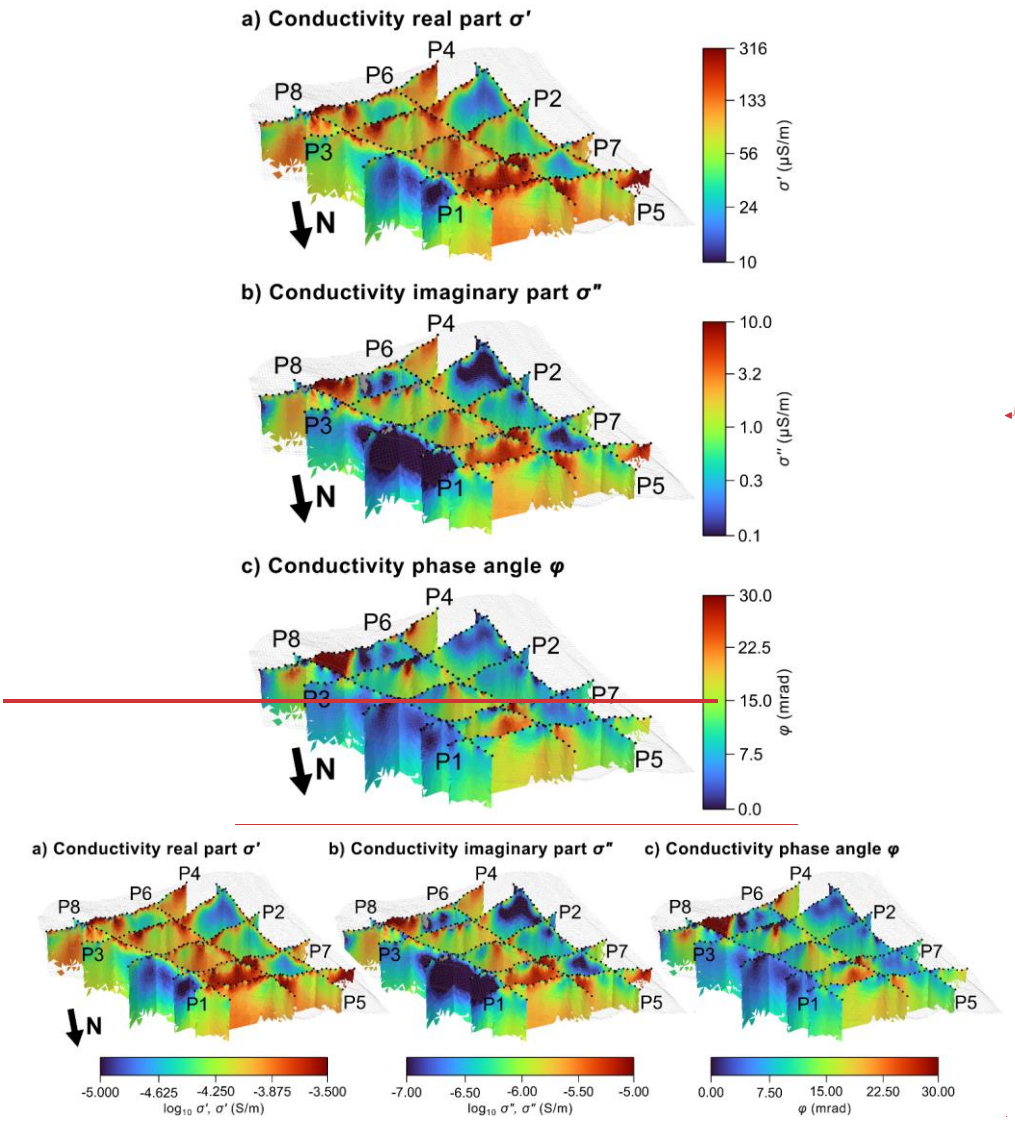

Formatiert: Zentriert

Figure 23: Slices of the 3D inverse model along the profiles at 0.5 Hz in terms of a) real part, b) imaginary part and c) phase angle of the complex conductivity. The north direction is given by a black arrow. The positions of electrodes are indicated by black dots.

~~While the electrical properties along P5 and P8 are horizontally layered with a relatively continuous permafrost layer, we can observe higher spatial variability in the center of the rock glacier, at the position where both the white and the black lobe intersect. Such area is covered by all profiles apart from P5 and P8 and can be characterized by maximum values in σ' and σ'' in all layers. As discussed later, the higher σ' and σ'' values in this area may be due to a lower and only sporadic ice content, the accumulation of finer materials, as well as due to water flowing internally along the rock glacier.~~

3.2 Estimation of hydrogeological parameters based on IP data

~~To estimate water content θ and hydraulic conductivity K based on the DSLM in the Gran Sometta rock glacier, we calculated M_n as the difference between the conductivity real part at 25 Hz and 0.1 Hz of the MG inverse model using equation 8 proposed in Revil et al. (2020). However, this equation is only valid in the case of a constant phase angle and a linear relation between M_n and σ''. In our case, the linear relation between M_n and σ'' is weak (see Fig. 3c) with a large contrast between the predicted and the estimated slope α (10.11 and 3.37). Such discrepancy is due to the strong increase of φ and the non-linear increase of $|\sigma^*|$ at frequencies above 2.5 Hz as presented in Fig. 3a (here marked as 'High frequency range'). Above 2.5 Hz, the surface conductivity is not only controlled by the accumulation and polarization of charges within the EDL at the grain-fluid interface, but also at the ice-water interface as observed by Stillman et al. (2010). The contribution of ice to the polarization at high frequencies is not considered in the DSLM (Coperey et al., 2019); thus, we decided to calculate M_n based on the conductivity resolved at 0.1 and 2.5 Hz (in Fig. 3a marked as 'Low frequency range'). As presented in Fig. 3b, such analysis results in a stronger correlation between M_n and σ'' with similar predicted and estimated values for α (2.06 and 1.91). However, the smaller the frequency window for the calculation of M_n is, the higher is the probability of overlooking polarization effects at higher frequencies, apart from ice polarization.~~

Kommentiert [CM3]: PART 2

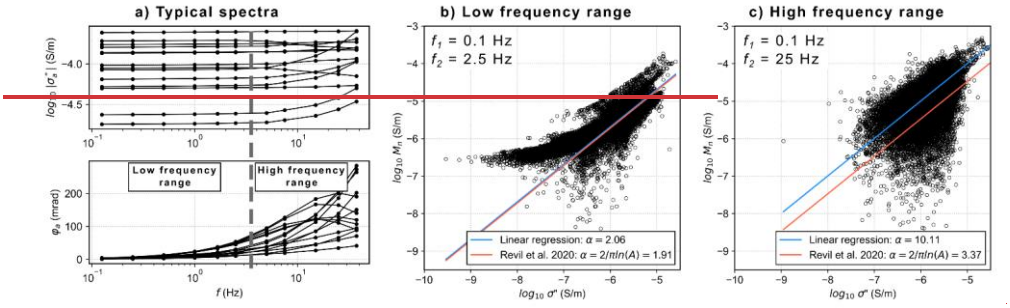

~~**Figure 3: a) Typical spectra of the apparent conductivity magnitude and phase shift of the Gran Sometta rock glacier. b) and c) present the relation between the normalized chargeability, calculated from a low frequency f_1 and a high frequency f_2, and the imaginary part of the complex conductivity at the geometric mean frequency between f_1 and f_2, for the low frequency (b) and the high frequency range (c). The blue line indicates a linear regression, while the red line represents the theoretical relation (Revil et al., 2020). The data shown here were collected with a MG configuration along P1-P8.**~~

The results for θ and K based on the DSLM are presented in Fig. 4 as slices parallel to the surface, in a depth of 4 and 20 m, as resolved from the 3D inversion. In the Appendix (Fig. ~~A3~~C1) we added the same slices in terms of ~~the~~ σ' ~~conductivity~~ at 0.1 Hz and ~~-~~M_n ~~the normalized chargeability~~. The water content is in a range of 0-15% (see Fig. 4a and 4b), and the hydraulic conductivity in a range of 10^{-7} to 10^{-3} m/s. Minimum values of both parameters (θ < 5% and K < 10^{-6} m/s) occur along P5 and P8 at a depth of 20 m, most likely because in this area most of the water is permanently frozen hindering water flow and leading to a low σ' and low σ'' at 0.5 Hz, as shown in Fig. ~~3~~2. We can observe higher θ and K values in the 4 m depth slice (K up to $10^{-4.5}$ m/s and θ up to 10%), which is unfrozen~~; and thus, allows water flow~~. Maximum θ values (up to 15%) can be observed in the western part of the white lobe (center of the rock glacier), not only in the ~~active layer~~uppermost layer close to the surface (4 m depth slice), where the rock glacier thaws during summer, but also at a depth of 20 m. ~~Both σ' and σ'' images (c.f., Fig. 2) indicate no continuously frozen layer in this area; thus, water can infiltrate from the uppermost layer in deeper areas and accumulates. The high values in both σ' and σ'' suggest the accumulation of fine grains in this area that reduces hydraulic conductivities and permits the water to be stored.~~

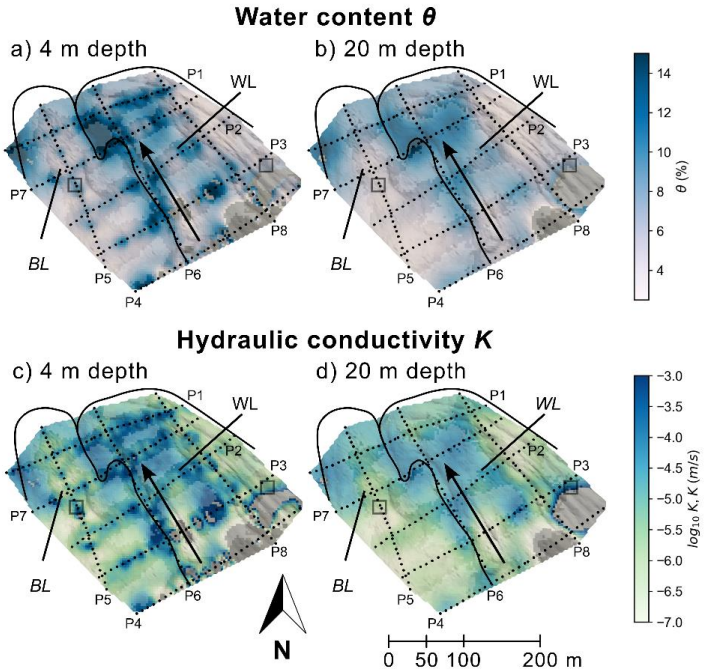

Figure 4: Water content (a and b) and hydraulic conductivity (c and d) visualized as slices parallel to the surface in two different depths. The edges of the black lobe (BL) and white lobe (WL) are indicated by black lines. Low sensitivity areas are displayed transparently, and the positions of electrodes are presented by black dots. Additionally, the direction of topography is indicated by a black arrow and the positions of tracer experiments by gray squares.

3.3 Tracer experiments

Figure 5 presents the 3D inversion results of the small-scale tracer experiments at the white lobe (left) and the black lobe (right). The baseline (time step 0) ~~electrical conductivity~~ σ' is visualized as slices along the two parallel electrode lines for the white lobe in Fig. 5a and for the black lobe in Fig. 5g. In the former, Fig. 5a reveals two layers, an upper relatively conductive layer ($\sigma' > $ ~~$10^{4.25}$~~56 µS/m), ~~which corresponds to the unfrozen active layer,~~ and a lower continuous resistive layer ($\sigma' <$ ~~$10^{4.25}$~~56 µS/m)~~, which is frozen and corresponds to the permafrost~~. The interface between both layers is at a depth of approximately 4 m, where also borehole temperature data show the interface between an unfrozen active layer and an underlying frozen layer ~~(in agreement with borehole temperature data presented in Fig. A2)~~ (4-6 m; see Fig. B1~~.~~). Therefore,

we assume that the upper conductive layer is the active layer and the lower resistive layer the frozen layer. The σ' baseline slices on the black lobe show the two layers as well but we can observe that the contrast between the upper conductive and the lower resistive layer is weaker, and the depth of the interface varies along the parallel profiles. The comparison of Fig. 5a and 5g, reveals that the black lobe is related to slightly higher electrical conductivity ~~values~~ in the ~~active~~ upper layer, although we observed similar θ values in the active layer of the black and white lobe (see Fig. 4a).

Time-lapse conductivity changes ($\Delta\sigma'$) after the saltwater injection in the center between the monitoring lines are presented in Fig. 5b-5f (white lobe) and 5h-5l (black lobe). Blue colored voxels present a $\Delta\sigma'$ of $\geq$ +40% (white lobe) and $\geq$ +20% (black lobe) compared to the baseline σ'. Different thresholds (20% and 40%) were used because in the white lobe maximum values of $\Delta\sigma'$ were in a range of +200%, in the black around +50%. In the white lobe, during and directly after the injection, a conductive anomaly ($\Delta\sigma' > 40\%$) propagates from the injection point downwards nearly perpendicular to the gravitational field. After reaching the interface between the active and the frozen layer, the anomaly starts to move through the active layer parallel to the interface. In the black lobe, we can also observe a change in conductivity starting from the injection point, but the value is smaller (~20-30%, with maxima around 50%). The conductive anomaly percolates nearly vertically from the injection point, similar to the movement in the white lobe directly after the injection, yet, the conductive plume stops at a distance of 2-3 m below the injection point and no movement downslope is observed, in contrast to the lateral movement observed in the white lobe.

The TLBC inversion results of the large-scale tracer experiment on the black lobe are visualized in Fig. D1. The results show a $\Delta\sigma'$ anomaly moving from the injection point downslope along the surface. In comparison to the small-scale tracer tests, the $\Delta\sigma'$ plume is much smaller (~5% compared to ~20% and ~40%, respectively) most likely due to the different sensitivity associated with the larger electrode separation used in the large-scale tracer experiment (5 m vs. 2 m). In the images, the smaller $\Delta\sigma'$ values in the downslope vicinity of the injection point highlight conductivity changes associated to inversion artifacts, as can be observed particularly in the area above the injection point, where we do not expect big changes over time. ~~Hence, the high σ' values resolved in the black lobe indicate a higher content of fine grains filling large pores related to a significant contribution of surface conductivity.~~

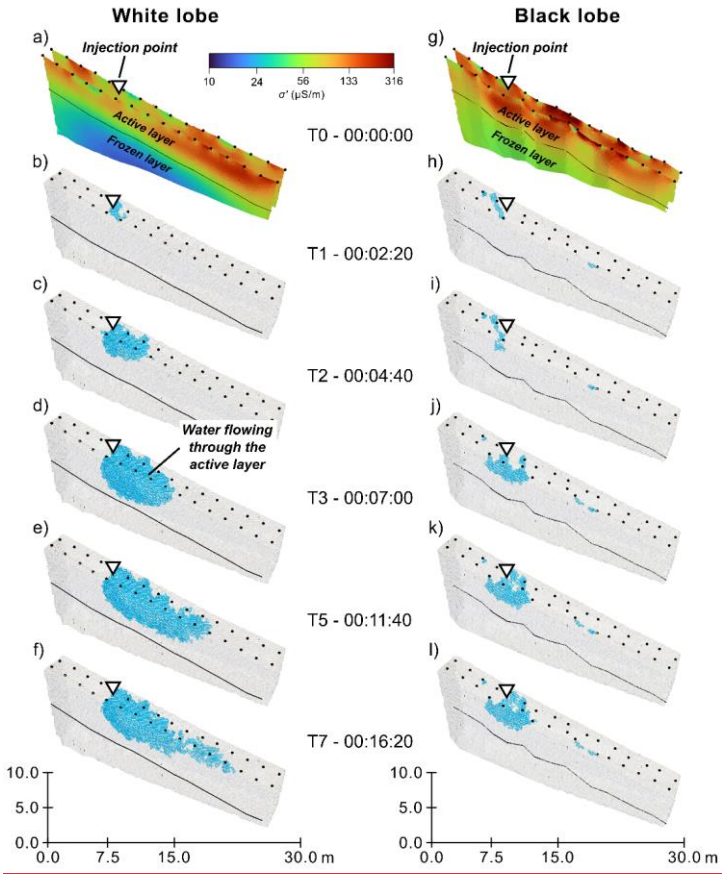
White lobe
Black lobe
a)
g)
Injection point
Injection point
10
24
56
133
316
σ' (µS/m)
Active layer
Frozen layer
Active layer
Frozen layer
T0 - 00:00:00
b)
h)
T1 - 00:02:20
c)
i)
T2 - 00:04:40
d)
j)
Water flowing through the active layer
T3 - 00:07:00
e)
k)
T5 - 00:11:40
f)
l)
T7 - 00:16:20
10.0
5.0
0.0
0.0
7.5
15.0
30.0 m
10.0
5.0
0.0
0.0
7.5
15.0
30.0 m

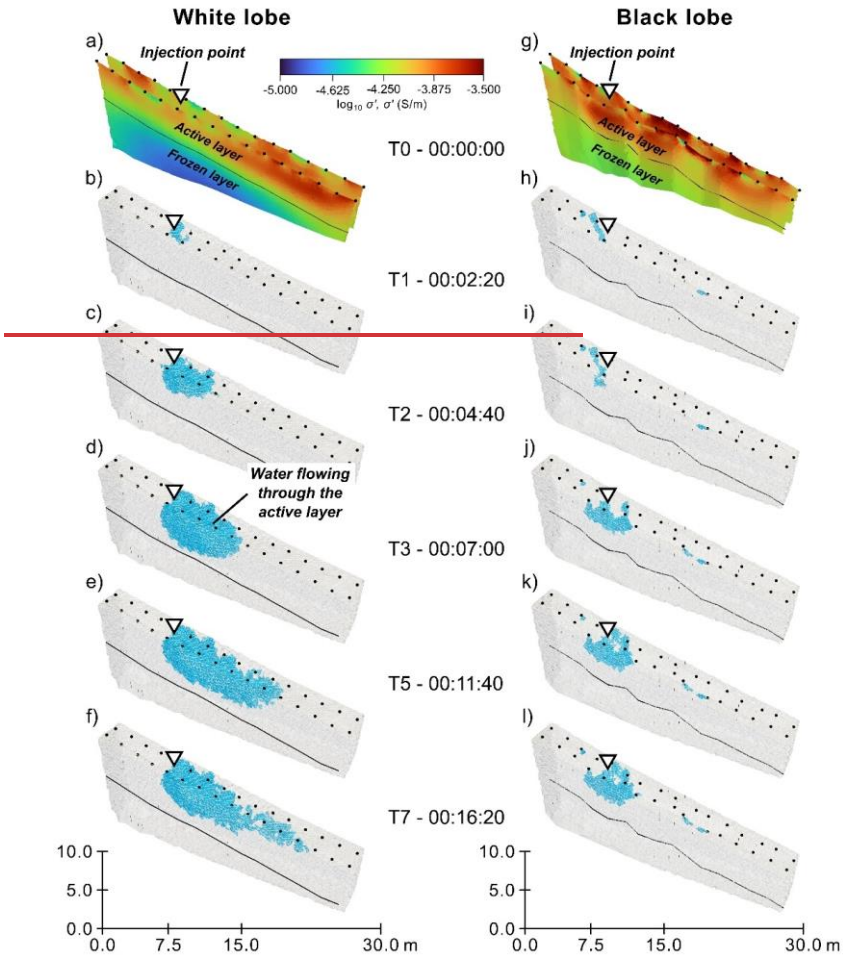

Figure 5: Slices presenting the real part of the complex conductivity along the electrode lines at the baseline for the white lobe (a) and black lobe (g). The black line indicates the interface between the active layer and the frozen layer, determined and interpreted by the gradient ~~of~~ in the electrical conductivity model. b) to f) and h) to l) represent the change of the conductivity with time after the injection of a salt tracer. Blue areas show a conductivity increase above

40% in the case of the white lobe and above 20% in the case of the black lobe. The position of the tracer injection is indicated by a triangle, while the positions of electrodes are indicated by black dots. A scale was added on the bottom.

~~The movement of the saltwater, injected in the center between the monitoring lines, can be resolved by means of the time-lapse changes in the ERT monitoring imaging results presented in Fig. 5b-5f (white lobe) and 5h-5l (black lobe). Blue colored voxels present a σ' increase of ≥ 40% (white lobe) and ≥ 20% (black lobe) compared to the baseline σ'. In the white lobe, during and directly after the injection, the water propagates from the injection point downwards nearly perpendicular to the gravitational field. After reaching the interface between the active and the frozen layer, the saltwater starts to flow through the active layer parallel to the interface. In the black lobe, the water percolates nearly vertically from the injection point, similar to the water movement in the white lobe directly after the injection. However, in the black lobe the saltwater plume stops at a distance of 2–3 m below the injection point and no flow downslope is observed; thus, suggesting a lower hydraulic connectivity in the black than in the white lobe (see discussion in section 4.1).~~

~~Changes in the electrical conductivity over time (after the injection of the tracer) permits to estimate the velocity of the water moving through the subsurface, as presented in Fig. 6a. Singha and Gorelick (2005) and Camporese et al. (2011) demonstrated that the timing of the peak arrival is a reliable parameter for K estimations because it is relatively unaffected of inversion artifacts. Hence, we used the time of the maximum conductivity concentration in 18 voxels to estimate the arrival time of the saltwater in the given voxels. Skipping the inversion and estimating K based on raw data can lead to wrong interpretations, considering that the raw data does not contain information about the spatial position of the anomaly (Camporese at al., 2011). As presented in Fig. 6a and 6c, the time t of the maximum $\Delta\sigma$, also called arrival time T_a, increases with increasing distance from the injection position as the tracer moves from the injection position downslope through interconnected pores in the active layer. Additionally, we can observe that the slope of T_a – $\Delta\sigma$ is not constant over a distance of 0–23 m from the injection position but reveals a contrast between the nearest voxels and voxels which are further away from the injection position. This contrast reflects the two different flow characteristics identified in Fig. 5: An initial nearly vertical flow (from now on called stage 1, S1) followed by a flow parallel to the interface between the active layer and the frozen layer (from now on called stage 2, S2).~~

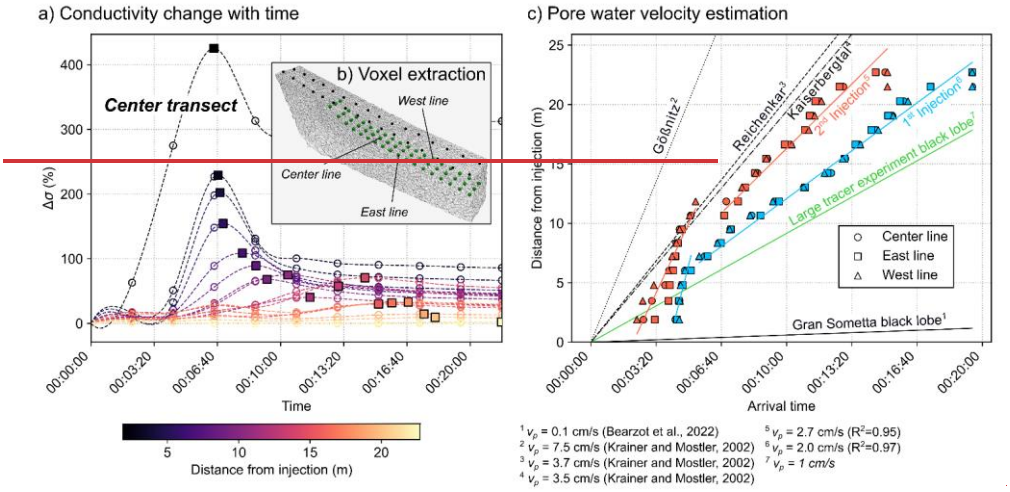

~~**Figure 6: a) Change of the conductivity in % with time relative to the baseline for different voxels (positions are presented in b)) along the center line of the tracer path in the active layer. The distance of the voxel from the injection position is presented by the line color, the maximum change of conductivity for each voxel is visualized by a square symbol. c) shows the time of the maximum change of conductivity for each voxel in relation to the distance from the injection point. The slope of a linear regression (in blue for injection 1, in red for injection 2) gives the pore water velocity. Pore water velocities of other studies are visualized by the black lines for a comparison. The estimated pore water velocity in the large-scale tracer experiment on the black lobe is added in green.**~~

~~The pore water velocity v_p, which was estimated by the slope between T_a and the distance from the injection point, is presented in Fig. 6c. Due to the different slopes observed in Fig. 6a we fit two linear regression models per tracer injection, one for S1 and one for S2, resulting in a v_p of 10.9 cm/s (injection 1) and 5.9 cm/s (injection 2) for S1 and a v_p of 2.0 cm/s (injection 1) and 2.7 cm/s (injection 2) for S2. The contrast in v_p between S1 and S2 is mainly related to the difference in the hydraulic gradient, while the discrepancy in v_p between injection 1 and injection 2 is related to a difference in the matrix potential. When we injected saltwater for the second time the subsurface materials were already wet from the previous injection (higher θ). The higher water content during the second injection leads to a lower absolute matrix potential and in turn to higher K and v_p values (e.g., Van Genuchten, 1980). Additional lines in Fig. 6c present results from different studies and will be discussed in section 4.2.~~

~~The TLBC inversion results of the large-scale tracer experiment on the black lobe are visualized in Fig. A4. In comparison to the small-scale tracer tests, the changes in the electrical conductivity close to the injection point and downslope were much smaller (~5% compared to ~20% and ~40%, respectively) most likely due to the different sensitivity associated with the larger electrode separation used in the large-scale tracer experiment (5 m vs. 2 m). In the images, the smaller changes in electrical conductivity associated with the tracer highlight conductivity changes associated to inversion artifacts, as can be observed particularly in the area above the injection point, where we do not expect big changes over time. Only interpreting the increase of electrical conductivity from the injection point along the surface downslope, the inversion images suggest a pore water velocity of around 1 cm/s (see green line in Fig. 6c). However, this value is not as reliable as the one derived from the small-scale tracer experiment on the white lobe due to time-lapse inversion artifacts.~~

3.4 Rock glacier movement

Figure ~~7~~6 presents the direction and magnitude of the horizontal displacement of 161 rocks on the surface of the Gran Sometta rock glacier between August 2022 and August 2023 as determined from the kinematic analysis of the UAV images (see section 2.7). The kinematic changes of the rock glacier surface over the longer time span (2020-2023) are presented in Fig. ~~A5~~ E1 (Appendix). Most parts of the rock glacier moved to the northwest due to the aspect of the surface topography, except for a few points at the lateral boundaries of the rock glacier lobes. Over the whole area under investigation, the displacements are between 0 and 2 m per year, with a higher range of values on the black lobe (1-1.5 m/y) than on the white lobe (0-0.5 m/y). Maximum values can be observed on the southern part of the black lobe (> 1.5 m/y), while the minimum displacements (< 0.25 m/y) were measured on the front and eastern part of the white lobe.

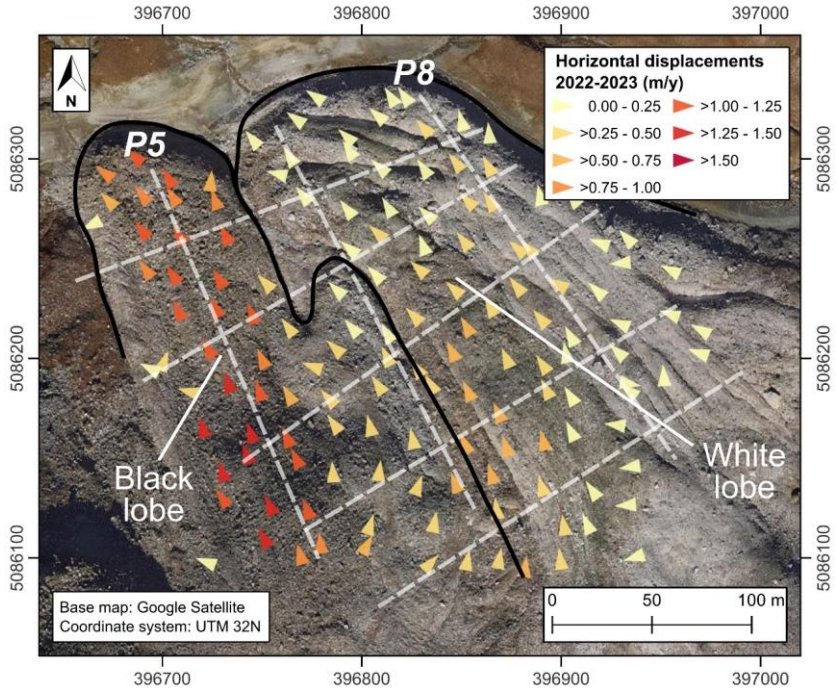

Figure ~~7~~ 6: Horizontal displacements of the Gran Sometta rock glacier between 2022 and 2023. The direction of the arrows presents the direction of the rock glacier movement, while the color displays the velocity of the rock glacier in m/yr. The positions of the SIP profiles are indicated by white dashed lines, while the front edge of the rock glacier and the border between the black and the white lobe are presented by a black line. Orthophoto: © Google Earth 2022.

4 Discussion

4.1 Identifying hydraulic units in the Gran Sometta rock glacier

Based on the complex conductivity results presented in Fig. 3 we identified three layers along the white and the black lobe. The relatively conductive, in comparison with the underlying second layer, uppermost layer is related to the active layer with a thickness of 4-6 m, in this case associated with unfrozen sediments and rocks (as described in Bearzot et al., 2022). No direct validation data of active layer thickness for the measurements in 2022 and 2023 is available because boreholes with

hat formatiert: Nicht Hervorheben

hat formatiert: Nicht Hervorheben

temperature sensors in the Gran Sometta rock glacier were destroyed in 2018. However, the active layer thickness estimation is in a similar range as the value determined from the boreholes (6 m in borehole 1 and 4 m in borehole 2) during 2015-2016 (see Fig. B1). We expect an active layer thickness in 2022 still in a range between 4 and 6 m as rock glaciers are more resilient towards increasing air temperatures compared to other permafrost features (e.g., Pruessner et al., 2021). The second layer is more resistive than the uppermost layer corresponding to the frozen materials with a thickness of 20-30 m, in agreement with results from Bearzot et al. (2022). At a depth of 20-30 m the conductivity increases again, which indicates the lower bound of the permafrost or a decreased ice content.~~related to unfrozen sediments and rocks in the active layer with a thickness of approximately 4–6 m, in this case associated to blocky but also fine-grained materials (Bearzot et al., 2022). No direct validation data of active layer thickness for the measurements in 2022 and 2023 is available because boreholes with temperature sensors in the Gran Sometta rock glacier were destroyed in 2018. However, the active layer thickness estimation is in a similar range as the value determined from the boreholes (6 m in borehole 1 and 4 m in borehole 2) during 2015–2016 (see Fig. A2). We expect an active layer thickness in 2022 still in a range between 4 and 6 m as rock glaciers are more resilient towards increasing air temperatures compared to other permafrost features (e.g., Pruessner et al., 2021).~~

~~corresponding to the frozen materials with a thickness of 20–30 m, in agreement with results from Bearzot et al. (2022). The bottom layer corresponds to the unfrozen materials related to higher electrical conductivity and polarization values (i.e., σ' and σ'').~~

In this study, we applied the model proposed by Soueid Ahmed et al. (2020) (explained in section 2.4, see Eq. (13)), based on the DSLM developed by Revil (2013a,b), to estimate K on the Gran Sometta rock glacier. The results show a contrast in K values between the unfrozen active layer (K up to 10^{-3} m/s) and the frozen layer (K down to 10^{-7} m/s). Such contrast in K values is in agreement with results of the tracer test in the white lobe. We assume that the conductive anomalies changing their position observed in the tracer experiments are due to the saltwater plume moving through the subsurface (c.f., Fig. 5). ~~, where we injected saltwater on the surface and monitored associated spatio-temporal changes through 3D time-lapse electrical conductivity monitoring.~~ The time-lapse inversion images in the white lobe ~~(c.f., Fig. 5)~~ suggest that, after a nearly vertical flow in the uppermost 3 m, the injected water was blocked by a resistive layer, associated with a frozen ice-rich ~~frozen~~ layer. This layer might hinder the infiltration of most of the water into deeper areas along the tracer test site on the white lobe, which leads to a nearly parallel flow to the interface between the frozen layer and the active layer.

~~On the black lobe, we conducted two tracer experiments with two different scales.~~ In the small-scale experiment in the black lobe (c.f., Fig. 5), the injected water spread a few meters around the injection point but did not move further downslope. Compared to the tracer test area on the white lobe, we observed bigger blocks on the black lobe with huge pores and a poor hydraulic connection. We suggest that we did not inject enough water (70 l per injection) to hydraulically connect such big pores; thus, the water might have been run through the uppermost hollow spaces, split up in different holes and stopped there. Additionally, the conditions during the tracer experiment in the black lobe in August 2023 were drier than during the tracer test in the white lobe in October 2022, which also leads to a lower hydraulic connection between pores. The saltwater injected in the large-scale tracer experiment in the black lobe has been successfully tracked in the inversion images (c.f., Fig. ~~A4~~D1)

hat formatiert: Nicht Hervorheben

hat formatiert: Nicht Hervorheben

hat formatiert: Nicht Hervorheben

Formatiert: Standard

but the results need to be considered carefully due to time-lapse inversion artifacts observed along the profile. The images reveal a similar water flow as observed in the small-scale tracer experiment in the white lobe with a nearly parallel flow to the surface through the active layer.

The water flow resolved with electrical images described above is in agreement with the assumption that frozen areas in active rock glaciers act as impermeable layers hindering water flow (e.g., Krainer and Mostler, 2002; Giardino et al., 2011; Winkler et al., 2016 and Del Siro et al., 2023). Commonly, the dispersion of a tracer is monitored through chemical analyses of samples from several sampling points, e.g., boreholes or springs. Krainer and Mostler (2002) e.g., conducted hydrological tracer experiments on rock glaciers in Austria, where the time between the tracer injection and the arrival time at the rock glacier spring allows to measure a mean pore water velocity, which resulted in relatively large flow velocities. Given that frozen materials are rather poor hydraulic conductors (e.g., Burt and Williams, 1976) and the active layer mainly consists of large blocks with huge pores with a high hydraulic conductivity, the authors suggested that the water does not percolate into the frozen layer but flows through the active layer. Whereas sampling provides highly accurate and reliable data, such information gives only discrete information about the tracer flow and can fail if the tracer escapes from the sampling points (Cassiani et al., 2006). Coupling tracer experiments with time-lapse ERT monitoring overcomes this limitation as the method provides continuous images of the subsurface over time, which can be used to describe the movement and the dispersion of the fluid (e.g., Camporese et al., 2011).~~However, such tracer tests do not provide information about the actual flow path of the tracer.~~ Recently, Pavoni et al. (2023~~b~~) conducted a tracer experiment in the inactive Sadole rock glacier, where they tracked the position of a salt tracer by a 2D ERT monitoring over a distance of 40 m. They reported that most of the water did not percolate into the frozen area but moved through the active layer.

Bearzot et al. (2022) injected a tracer fluid in the black lobe of the Gran Sometta rock glacier and measured the arrival time at the spring located at a distance of around 270 m down gradient. The arrival of the tracer was identified by changes in the chemical composition of the spring water, and estimations of the pore water velocity were conducted through the distance between the injection point and the spring position divided by the elapsed time. Their analyses in the black lobe resolved a pore water velocity of around 10^{-3} m/s but they only monitored the chemical composition of the spring water during the night, which might have led to an underestimation of the pore water velocity. The value is smaller than the pore water velocities estimated by Krainer and Mostler (2002) ($v_p \sim 10^{-2}$) for three rock glaciers in Austria ~~(see Fig. 6)~~, but still suggests that the water mainly ~~flew~~ flowed through the active layer.

4.2 Hydraulic conductivity estimation based on tracer experiments ~~and multi-frequency electrical conductivity~~

The $\Delta\sigma'$ anomalies detected in Fig. 5 in the white and black lobe are moving from the injection point downslope directly after the time of the injection. Therefore, we assume that the increase of σ' ($\Delta\sigma'$ anomaly) is related to the injected saltwater, which moves through the active layer of the rock glacier. Changes in σ' over time (after the injection of the tracer) permits to estimate the velocity of the water moving through the subsurface, as presented in Fig. 7a for the white lobe. For the small tracer

experiment in the black lobe we did not conduct such an analysis because the conductive anomaly associated with the injected saltwater stopped 2-3 m below the injection point.

Singha and Gorelick (2005) and Camporese et al. (2011) demonstrated that the timing of the peak arrival is a reliable parameter for K estimations because it is relatively unaffected by inversion artifacts. Hence, we used the time of the maximum conductivity concentration in 18 voxels to estimate the arrival time of the saltwater in the given voxels. Skipping the inversion and estimating K based on raw data can lead to wrong interpretations, considering that the raw data does not contain information about the spatial position of the saltwater plume (Camporese at al., 2011). As presented in Fig. 7a and 7c, the time t of the maximum $\Delta\sigma'$, also called arrival time T_a, increases with increasing distance from the injection position as the tracer moves from the injection point downslope through interconnected pores in the active layer. Additionally, we can observe that the slope of $T_a - \Delta\sigma'$ is not constant over a distance of 0-23 m from the injection position but reveals a contrast between the nearest voxels and voxels which are further away from the injection position. This contrast reflects the two different flow characteristics identified in Fig. 5: An initial nearly vertical flow (from now on called stage 1, S1) followed by a flow parallel to the interface between the active layer and the frozen layer (from now on called stage 2, S2).

The pore water velocity v_{p_a} which was estimated by the slope between T_a and the distance from the injection point, is presented in Fig. 7c. Due to the different slopes observed in Fig. 7a we fit two linear regression models per tracer injection, one for S1 and one for S2, resulting in a v_{p_a} of 10.9 cm/s (injection 1) and 5.9 cm/s (injection 2) for S1 (mean value: 8.4 cm/s) and a v_{p_a} of 2.0 cm/s (injection 1) and 2.7 cm/s (injection 2) for S2 (mean value: 2.35 cm/s). The contrast in v_{p_a} between S1 and S2 is mainly related to the difference in the hydraulic gradient, while the discrepancy in v_{p_a} between injection 1 and injection 2 is related to a difference in the matrix potential. When we injected saltwater for the second time the subsurface materials were already wet from the previous injection (higher θ). The higher water content during the second injection leads to a lower absolute matrix potential and in turn to higher K and v_{p_a} values (e.g., Van Genuchten, 1980).

hat formatiert: Nicht Hervorheben

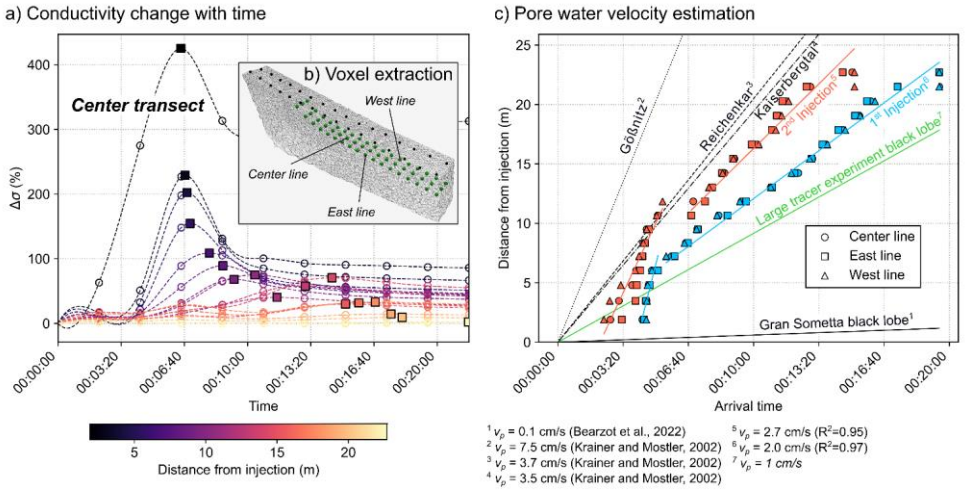

Figure 7: a) Change of the conductivity in % with time relative to the baseline for different voxels (positions are presented in b)) along the center line of the tracer path in the active layer during the small-scale tracer experiment in the white lobe. The distance of the voxels from the injection position is presented by the line color, the maximum change of conductivity for each voxel is visualized by a square symbol. c) shows the time of the maximum change of conductivity for each voxel in relation to the distance from the injection point. The slope of a linear regression (in blue for injection 1, in red for injection 2) gives the pore water velocity. Pore water velocities of other studies are visualized by the black lines for a comparison. The estimated pore water velocity in the large-scale tracer experiment on the black lobe is added in green.

~~Only interpreting the increase of electrical conductivity from the injection point along the surface downslope, the inversion images suggest a pore water velocity of around 1 cm/s (see green line in Fig. 6c). However, this value is not as reliable as the one derived from the small-scale tracer experiment on the white lobe due to time-lapse inversion artifacts.~~

~~Based on the arrival times of the tracer and the time elapsed, we estimated the pore water velocity v_p in the white lobe for the two stages (c.f., Fig. 6c), resulting in values of 8.4 cm/s (S1) and 2.35 cm/s (S2) respectively (mean value over injection 1 and injection 2).~~ Multiplying the mean values of v_p for S1 and S2 with the reciprocal of the hydraulic gradient (0.57 for S1 and 4.77 for S2) and an assumed mean porosity of 40% (as used in other rock glacier studies, e.g., Hauck et al., 2011; Halla et al., 2021) allows us to estimate the hydraulic conductivity, which results in K values of 1.9×10^{-2} m/s (S1) and 4.5×10^{-2} m/s (S2). The difference in the values resolved for the two stages is related to vertical changes in the water content in the active layer of the rock glacier. While the uppermost rocks in the active layer (S1) are relatively dry, the material at the interface

between the frozen layer and the active layer (S2) can assumed to be more humid leading to the slight increase of K in S2. The hydraulic gradient used in S1 was derived from the slope of the water path in Fig. 5, while the hydraulic gradient in S2 was derived from the topography gradient because the tracer experiment images (c.f., Fig. 5) suggest that in S2 the water flowed along a frozen layer nearly parallel to the surface. Changing the porosity or the hydraulic gradient in a range between ±50% of the absolute value only slightly affects the estimation of K (see Fig. G1 in the Appendix) as the range of values for v_p and K can extend over several orders of magnitudes. ~~The difference in the values resolved for the two stages is related to vertical changes in the water content in the active layer of the rock glacier. While the uppermost rocks in the active layer (S1) are relatively dry, the material at the interface between the frozen layer and the active layer (S2) can assumed to be more humid leading to the slight increase of K in S2.~~

The large-scale tracer experiment on the black lobe permitted the computation of the pore water velocity (see Fig. ~~A4~~ D1 in the Appendix), resolving for values around 1 cm/s (see green line in Fig. ~~6~~7c), which is half of the v_p estimated for the white lobe, but needs to be considered carefully due to time-lapse inversion artifacts (as described in section 3.3). This lower pore water ~~hydraulic conductivity~~velocity found in the black lobe compared to the white lobe would explain the difference in water movement observed in the small-scale tracer experiments conducted on the white and the black lobe. However, the v_p value estimated by Bearzot et al. (2022) for the black lobe (based on the analysis of water samples at the rock glacier spring after the injection of a tracer fluid) is one order of magnitude lower than the value derived from our tracer experiment (10^{-3} m/s vs. 10^{-2} m/s). This discrepancy can be related to the difference in the covered flow path. While our ERT monitoring covered a steep area with a maximum length of only 30 m, Bearzot et al. (2022) investigated the flow over a distance of 270 m, covering also flat areas. Accordingly, the study area of Bearzot et al. (2022) might result in the averaged values from high pore water velocity in the steep areas (covered in our study) and the low pore water velocity in the flatter areas not investigated with our tracer test.

In Fig. ~~7~~6c, we also compare v_p estimations in our study with results from other rock glaciers based on hydrological tracer experiments. The v_p results for the Gößnitz, Reichenkar and Kaiserbergtal rock glaciers (located in the Eastern Alps) reveal v_p values varying between 3.5 to 7.5 × 10^{-2} cm/s (Krainer and Mostler, 2002). Those values are in the same order of magnitude as the value estimated for the white lobe with the small-scale tracer experiment and the value estimated in the large-scale tracer experiment in the black lobe. Variations in v_p between different rock glaciers can be related to different slope angles, geologies, active layer depths and ice content.

4.3 Uncertainty of hydrogeological properties estimated from multi-frequency electrical conductivity

In Fig. 4 we presented maps of θ and K estimated from multi-frequency electrical conductivity data. Comparing the K values from the tracer experiment in the white lobe with the results of K estimations for the active layer based on the analysis of the multi-frequency conductivity data (c.f., Fig. 4c) reveals a discrepancy of two magnitudes (10^{-2} m/s vs. 10^{-4} m/s). To understand

this discrepancy, it is useful to quantify the uncertainty in the estimated hydrogeological parameters from the geophysical imaging results. The petrophysical model to resolve θ and K from multi-frequency conductivity data requires different parameters, which are assumed to be constant across the entire rock glacier, namely, the fluid conductivity ($\sigma_f = 0.01$ S/m), the cementation exponent ($m = 2$), the grain density (2700 kg/m^3), the dimensionless parameter R (0.1), which relates M_n to σ_s, and the fitting parameter k_0 ($10^{4.3}$).

To investigate the uncertainty of θ and K, we (1) visualized the sensitivity of the parameters, and their standard deviations used in Eq. 12-14 on the resulting hydrogeological parameter (see Fig. 8), and (2) applied the error propagation law on Eq. 12-14. The equations used for the analysis regarding the error propagation and standard deviations of all parameters are given in Appendix F. The resulting values of θ due to variations in the assumed values of σ_f, R, and m (in an interval of $\pm$1 standard deviation) reveal that θ is primarily sensitive to σ_f (25.0% relative standard deviation, RSD) and m (17.0% RSD) and less sensitive to R (3.6% RSD), as presented in Fig. 8a-c. According to our analysis, the uncertainty of the parameters σ_f, R, and m results in an RSD of 30.5% for θ. The different sensitivities of the parameters highlight the need for an accurate estimation of particularly σ_f and m to derive a highly reliable water content.

In Fig. 8d-g we visualized the range of K considering $\pm$1 standard deviation of θ, ρ_g, CEC, and k_0. The parameters δ, g, and μ were fixed because we assume no strong deviation in these parameters. The strongest effect on K can be observed for θ (with a large RSD of 183%), followed by CEC (103% RSD), and k_0 (50% RSD), while the sensitivity of ρ_g is low (7.4% RSD) resulting in a total RSD of 216%. To obtain a more reliable hydraulic conductivity estimation, reducing the uncertainty of the water content and the CEC via more accurate information on σ_f and m is necessary. Additionally, there is a lack of information on the actual uncertainty and applicability of using a value of $10^{4.3}$ for the parameter k_0 (see Soueid Ahmed et al., 2020). Here, we used half of the value as standard deviation to investigate its sensitivity on the estimation of K.

The uncertainty in our results due to the non-uniqueness of the inversion itself and due to the imaging resolution related to the electrode spacing are not considered in the analysis above. In this study, we used an electrode separation of 7.5 m, which reduces the resolving capability of the electrical properties in the uppermost layer. An electrode spacing of 7.5 m was chosen as a compromise between a large depth of investigation (needed to cover the area below the permafrost), and a high resolution to resolve the active layer thickness, as well as to collect data over a large part of the rock glacier in a reduced time. Estimating the uncertainty of the inverse model is challenging (see list of approaches in Binley and Slater, 2020) because the inversion is an underdetermined problem, and therefore, beyond the scope of this manuscript. ~~Comparing the K values from the tracer experiment in the white lobe with the results of K estimations for the active layer based on the analysis of the multi-frequency conductivity data (c.f., Fig. 4c) reveals a discrepancy of two magnitudes (10^{-2} m/s vs. 10^{-4} m/s). Such a discrepancy might be most likely related to the enhanced hydraulic connectivity associated with the addition of water in the tracer experiments. Increasing the saturation enhances the interconnection between pores (e.g., Western et al., 2001); thus, resulting in higher K values. Moreover, the approach based on the analysis of multi-frequency conductivity data assumes a constant value in the~~

hat formatiert: Hochgestellt
hat formatiert: Hochgestellt
hat formatiert: Schriftart: Nicht Fett
hat formatiert: Nicht Hervorheben
hat formatiert: Nicht Hervorheben
hat formatiert: Nicht Hervorheben
hat formatiert: Schriftart: Nicht Fett
hat formatiert: Hochgestellt

~~fluid conductivity ($\sigma_f = 0.01$ S/m), the saturation exponent ($n = 2$) and cementation exponent ($m = 2$) across the entire rock glacier, as described by Soueid Ahmed et al. (2020) and Revil et al. (2020), while the analysis of the tracer test does not require such assumptions.~~ Additional uncertainty is due to the calculation of M_n in our study as we used a relatively small frequency window (0.1-2.5 Hz), which increases the risk of overlooking polarization effects at higher frequencies ($f > 2.5$ Hz), apart from ice polarization.

Accordingly, while our study reveals that the use of the DSLM might provide relevant information about the hydrogeological features and their connectivity, a quantitative estimation of hydrogeological parameters, par~~water content and~~ ticularly of the hydraulic conductivity, might ~~might~~ still require some calibration for its application. ~~Additionally, the variations in the estimated values might be related to the electrode spacing (7.5 m) used for the SIP mapping, which reduces the resolving capability of the electrical properties in the uppermost layer. An electrode spacing of 7.5 m was chosen as a compromise between a large depth of investigation (needed to cover the area below the permafrost), and a high resolution to resolve the active layer thickness, as well as to collect data over a large part of the rock glacier in a reduced time.~~ Future studies might consider approaches to estimate the uncertainty of the geophysical parameters and a more accurate estimation of σ_f, m, and k_0~~the collection of data with varying electrode spacing to improve hydrogeophysical investigations~~.

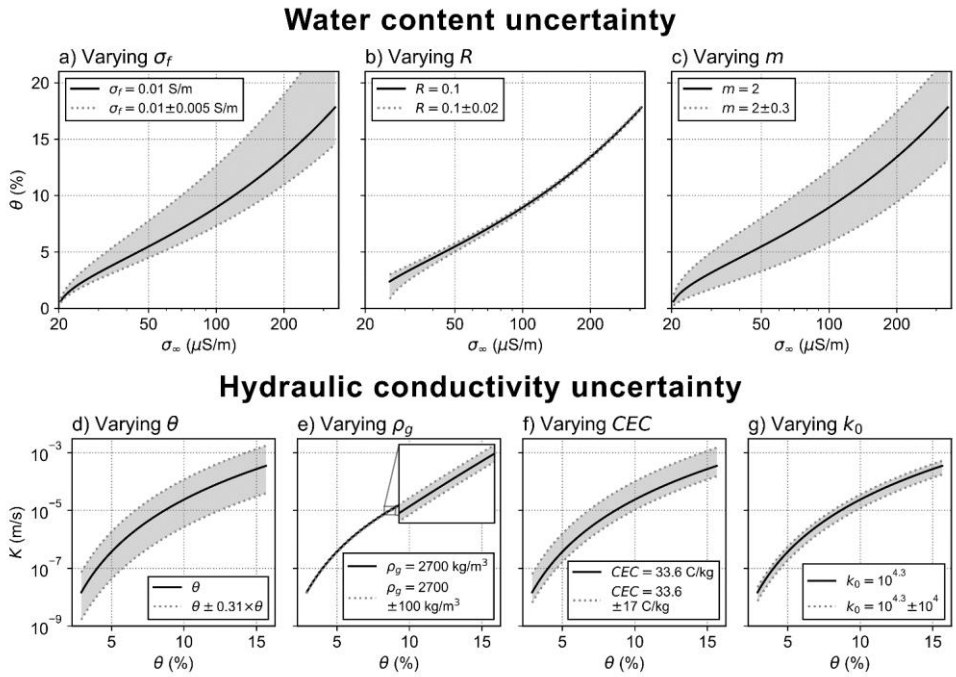

Figure 8: Uncertainty analysis of the hydrogeological parameters θ (a-c) and K (d-g). The black line symbolizes θ and K, respectively, in relation to the absolute values, while the gray area, limited by dotted lines, shows the range of θ and K using ±1 standard deviation (68% confidence interval) of the parameters used in Eq. 12-14. The range of values used in a)-c) for σ_∞ and θ was chosen based on the minimum and maximum of σ_∞ and θ in the 4 m and 20 m depth slices (c.f., Fig. 4). While we used a constant value for the tested parameters in subplots a)-c) and e)-g), we varied θ according to the values given in Fig. 4a,b and used a mean fractional standard deviation of 0.31, derived from error propagation for θ.

4.34 The large variability in water content and hydraulic conductivity at the Gran Sometta rock glacier

Results of the estimation of hydrogeological properties (θ and K) have shown a high spatial variability with depth and laterally across the rock glacier (c.f., Fig. 4). We can observe high θ values (up to 15%) in the active layer, where rain and snow meltwater can accumulate on top of the frozen layer. At a depth of 20 m, the rock glacier is frozen in several areas resulting in

a low amount of liquid water, and which hinders vertical water flow to deeper areas. Laterally, local maxima of θ can be found along furrows, particularly longitudinal furrows, while local minima can be found in ridges. Such spatial pattern suggests that water from snowmelt or rainfalls flows nearly vertically through the active layer, as described by S1 in the small-scale tracer experiments, until it reaches the interface between the active layer and the frozen layer. After that, in S2 the water moves along the interface downhill in direction of the steepest slope, either in flow direction of the rock glacier or into a near depression zone (see e.g., Halla et al., 2021), which are the most shaded areas on the rock glacier with low evaporation rates.

The longitudinal furrows act as preferential flow paths transferring water from areas above to the front part of the rock glacier (Halla et al., 2021) as the furrows are related to high hydraulic conductivity ($K > 10^{-4.5}$) (see Fig. 4c). After flowing through the furrows, water mainly accumulates in the western front part of the white lobe and can percolate into deeper areas (20 m depth) because there is no continuously frozen horizontal layer in such area. The complex conductivity results have revealed that the internal structure of the western frontal part of the white lobe is different compared to the eastern part of the white lobe and the black lobe. There is no continuous layer of low conductivity, associated with frozen materials, which might be related to a high ice-degradation rate allowing water to infiltrate into deeper areas, where we observed high θ values at a depth of 20 m, and which in turn accelerates the degradation process (Ikeda et al., 2008).

4.5~~4~~ Role of water content in the S~~s~~patial variability of rock glacier movement ~~is dominated by water content in the shear horizon~~

Several studies working on the kinematics of rock glaciers have revealed an overall acceleration of rock glacier movement during the last decades (e.g., Delaloye et al., 2010; Marcer et al., 2021; Kellerer-Pirklbauer et al., 2024). In some studies, variations in rock glacier velocities were related to the topography (e.g., Müller et al., 2016; Bodin et al., 2018), to the ice content (e.g., Kääb et al., 2007) or the thermal state (e.g., Bearzot et al., 2022) because, e.g., topographical variations and ground surface temperatures can be measured directly. Recent studies discuss the role of water content (e.g., Kenner et al., 2019), with a particular focus on the amount of liquid water in the shear horizon (e.g., Cicoira et al., 2019), where most of the deformation takes place (Arenson et al., 2002). However, due to the limited access, direct measurements of the water content in the shear horizon are challenging. Phillips et al. (2023) installed piezometers and an ERT monitoring in boreholes on a rock glacier in Switzerland that penetrate until the upper boundary of the shear horizon, permitting a direct investigation of the shear plane. They reported a link between high water content and increased rock glacier velocity for two seasons (Bast et al., 2024). Kinematic analyses on the Gran Sometta rock glacier have shown a contrast in surface velocities between the white and the black lobe, with higher values on the black lobe (~1-1.5 m/y) than on the white lobe (0-0.5 m/y) (c.f., Fig. 7 and ~~A4~~D1). ~~Such~~ This contrast is in agreement with kinematic results of similar analyses published by Bearzot et al. (2022) for the period 2016-2019 (~1.2 m/y for the black lobe and ~0.4 m/y for the white lobe). Bearzot et al. (2022) related the spatial flow patterns to the internal structure and the contrast in topography as the black lobe is ~~y~~steeper (~21° slope angle) than the white lobe (~11° slope angle). This suggestion is consistent with other rock glacier studies, which showed a strong link between slope angle and

surface velocity (e.g., Müller et al., 2016; Cicoira et al., 2021). ~~with a larger slope angle on the black lobe than on the white lobe.~~

The geophysically based estimation of the hydrogeological properties along both lobes in this study (see Fig. 9~~8~~) allows to investigate the relation between the water content and the spatial variations in rock glacier velocity.

Figure 9~~8~~c,g show that in the frozen layer most of the water is frozen in both lobes (θ < 5%) leading to a low electrical conductivity (see Fig. 9~~8~~a). Below this low electrical conductivity layer, we observe a layer of increased electrical conductivities associated with increased water content. In this area, higher θ is found for the black lobe (up to 10%) than for the white lobe (around 5%). Our results might indicate that water accumulates in the shear horizon of the black lobe at a profile distance above 100 m in southern direction, with higher K values (> 10^{-5} m/s) above 100 m profile distance than downslope (< 10^{-6} m/s) (see Fig. 9~~8~~d,h). The lower K ~~hydraulic conductivity~~ values may be due to a larger content of fine-grained sediments, as also suggested by the higher electrical conductivity and normalized chargeability values (Fig. ~~8~~9a,b). Such low K area might reduce the velocity of water flow coming from uphill leading to an increase in pore water pressure, which would in turn increase the potential of deformation in the shear horizon and can, together with the slope angle, ~~further~~ accelerate the rock glacier movement. This observation is similar to the one reported by Kenner et al. (2017) at the Ritigraben rock glacier, where borehole data revealed a wet area below the frozen layer at the depth of the shear horizon. Kenner et al. (2019) argue that the idea of water content as driving force for rock glacier kinematics is not a contradiction to the correlations between temperature and rock glacier velocity variations ~~temperatures~~ (Kääb et al., 2007; Roer et al., 2008), rather water content can act as the link between temperature and kinematic changes.

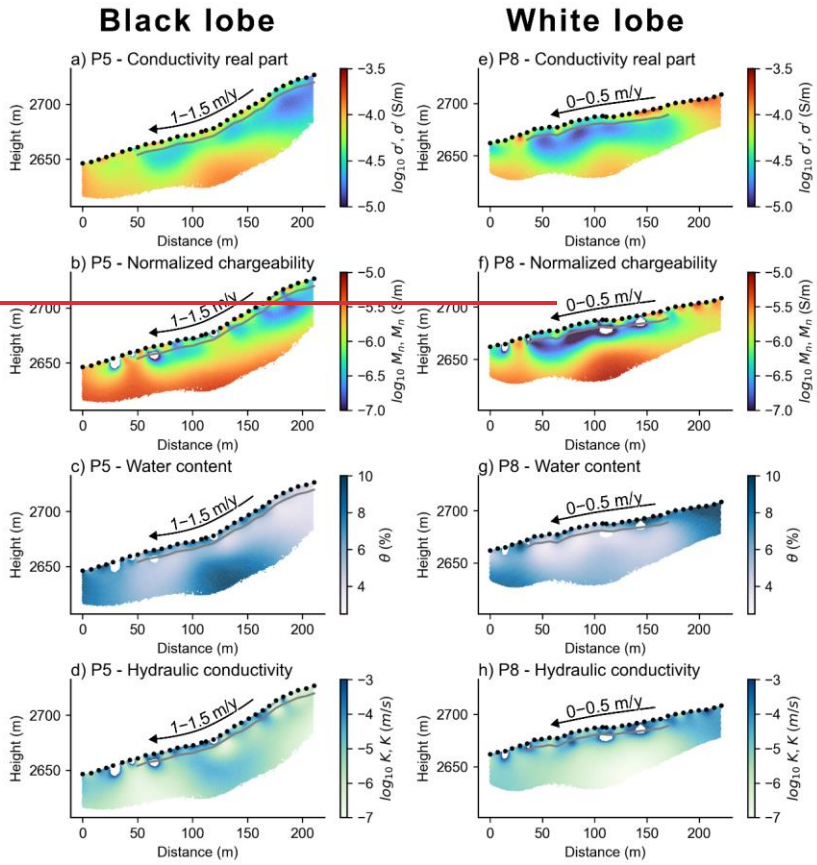
Black lobe
White lobe
a) P5 - Conductivity real part
e) P8 - Conductivity real part
b) P5 - Normalized chargeability
f) P8 - Normalized chargeability
c) P5 - Water content
g) P8 - Water content
d) P5 - Hydraulic conductivity
h) P8 - Hydraulic conductivity
1–1.5 m/y
0–0.5 m/y
Height (m)
Distance (m)
log10 σ′, σ′ (S/m)
log10 Mn, Mn (S/m)
θ (%)
log10 K, K (m/s)

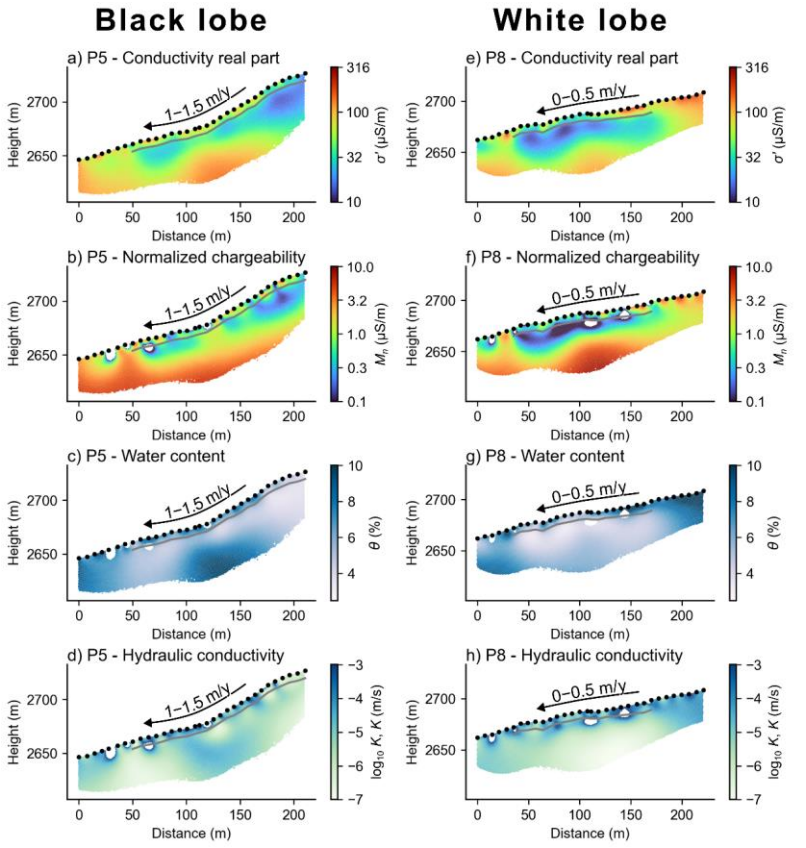

Figure 98: a) and e) show the real part of the complex conductivity, b) and f) the normalized chargeability, c) and g) the water content and d) and h) the hydraulic conductivity along P5 (left) and P8 (right). Pixels where the normalized chargeability results in negative values are blanked. The positions of electrodes are indicated by black dots, the interface between the active layer and the frozen layer is presented by a gray line. The rock glacier flow direction of each lobe is presented by a black arrow including its mean velocity.

5 Conclusions

In this study, we investigated the hydrogeological properties of the active Gran Sometta rock glacier in the Italian Alps by ~~an~~ SIP mapping. Electrical conductivity and normalized chargeability data were used within the DSL model to directly estimate the spatial water content and hydraulic conductivity distribution within the rock glacier. To validate the estimation of both parameters, we conducted tracer experiments, where we injected saltwater and tracked the change of electrical conductivity in the subsurface by an ERT monitoring. Both methods reveal similar hydraulic units: an upper non-frozen layer with high hydraulic conductivity and a lower frozen layer with low hydraulic conductivity. However, in the absolute values there is a discrepancy of two magnitudes between the hydraulic conductivity estimated within the DSL model and the tracer experiment, which is mainly related to the decreased resolution of the SIP mapping in the uppermost layer due to a large electrode spacing and the large uncertainty of the parameters used to estimate K. We observed that uncertainties in K estimations using the DSL model are strongly sensitive to the water content, which is in turn primarily sensitive to the fluid conductivity and the cementation exponent defined for the use of the petrophysical model.

The Gran Sometta rock glacier can be divided in three different areas characterized by their hydrogeological properties. As revealed by complex conductivity images, the internal structure of the black lobe and the eastern part of the white lobe is similar with an active layer of around 4-6 m thickness and a continuously frozen layer beneath, which is in agreement with borehole temperature data. The hydraulic conductivity and water content estimations based on the DSLM have shown that in both areas the frozen layer acts as a hydraulic barrier hindering water flow into deeper areas. Most of the water coming from rainfall or snowmelt flows rapidly through the active layer with hydraulic conductivities in a range of 10^{-2} m/s, with slightly higher values in the white lobe than in the black lobe, as revealed by the tracer tests. Contrary to this, in the western front part of the white lobe, ice content is low, and a continuously frozen horizontal layer is missing leading to water penetration into deeper areas where water accumulates in fine-grained sediments.

Additional analyses of the hydrogeological properties in the area below the poorly electrically conductive ice-rich layer have shown a higher water content in the black lobe (up to 10%) than in the white lobe (around 5%). As kinematic analyses have revealed that the black lobe moves three times faster than the white lobe, such contrast in water content suggests that water accumulated close to the shear horizon decreases the frictional resistance and in turn might accelerate the rock glacier velocity.

Our study shows that the ~~spectral induced polarization~~SIP method is a valuable tool to describe and quantify hydraulic conductivity and water content in rock glaciers. Such information does not only help in the understanding of the hydrological cycle in rock-glaciated alpine catchments, but it should also be considered in the analysis of spatial patterns in rock glacier movement.

Appendix A: 3D pseudosection

The 3D pseudosection of the apparent resistivity data after filtering along P1-P8 are shown in Fig. A1.

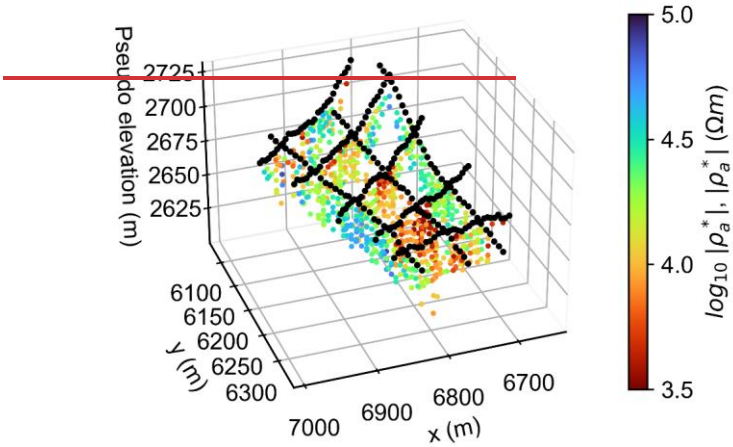

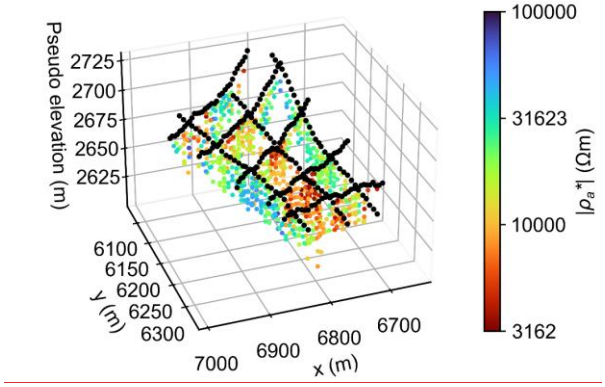

hat formatiert: Schriftart: Fett, Schriftfarbe: Automatisch

hat formatiert: Englisch (Vereinigte Staaten)

Formatiert: Standard

Figure A1: 3D visualization of the data along P1-P8 after the filtering procedure. The data are presented in terms of the apparent resistivity ($|\rho_a^*|$). Electrode positions are visualized as black dots.

Appendix B: Borehole temperatures

Temperature data from two boreholes in the Gran Sometta rock glacier are presented in Fig. B1~~A2~~. The active layer depth (ALD), which is the depth until the material thaws at least once per year, is ~6 m and ~4 m in borehole 1 and 2, respectively. The temperature data in borehole 1 shows that between 4 and 6 m depth the material does not freeze during winter, which suggests the existence of a supra-permafrost talik. Taliks have been observed several times in the European Alps (e.g., Zenklusen Mutter and Phillips, 2012; Luethi et al., 2017) and are assumed to be an indicator of permafrost degradation, but they have not been investigated in detail, yet. However, such information has not been reported at the Gran Sometta rock glacier. Nonetheless, as the temperature in the talik is close to the freezing point, we cannot exclude any calibration error in the temperature sensors, which could also lead to such temperature pattern.

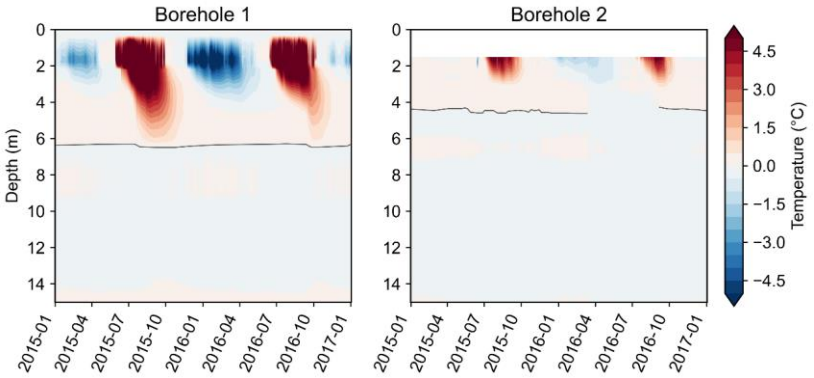

Figure ~~A2~~B1: Temperature data at two boreholes (borehole BH1 and borehole BH2) on the Gran Sometta rock glacier. The active layer depth is displayed by a gray line.

hat formatiert: Schriftart: Nicht Fett, Englisch (Vereinigtes Königreich)

Formatiert: Überschrift 1

Appendix C

: Conductivity real part and normalized chargeability maps

Figure C1 shows σ' and M_n used for the calculation of θ and K in a depth of 4 m and 20 m.

~~**Borehole temperatures**~~

~~Temperature data from two boreholes in the Gran Sometta rock glacier are presented in Fig. A2. The active layer depth (ALD), which is the depth until the material thaws at least once per year, is ~6 m and ~4 m in borehole 1 and 2, respectively. The temperature data in borehole 1 shows that between 4 and 6 m depth the material does not freeze during winter, which suggests the existence of a supra-permafrost talik. Taliks have been observed several times in the European Alps (e.g., Zenklusen Mutter and Phillips, 2012; Luethi et al., 2017) and are assumed to be an indicator of permafrost degradation, but they have not been investigated in detail, yet. However, such information has not been reported at the Gran Sometta rock glacier. Nonetheless, as the temperature in the talik is close to the freezing point, we cannot exclude any calibration error in the temperature sensors, which could also lead to such temperature pattern.~~

Formatiert: Überschrift 1

hat formatiert: Schriftart: Nicht Fett

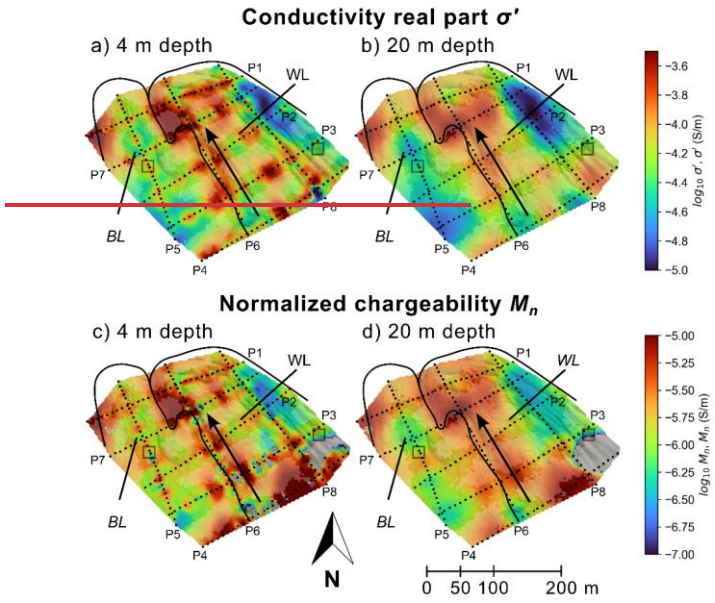
Conductivity real part σ'
a) 4 m depth
b) 20 m depth
P1
P2
P3
P4
P5
P6
P7
P8
WL
BL
−3.6
−3.8
−4.0
−4.2
−4.4
−4.6
−4.8
−5.0
log10 σ', σ' (S/m)
Normalized chargeability Mn
c) 4 m depth
d) 20 m depth
−5.00
−5.25
−5.50
−5.75
−6.00
−6.25
−6.50
−6.75
−7.00
log10 Mn, Mn (S/m)
N
0 50 100 200 m

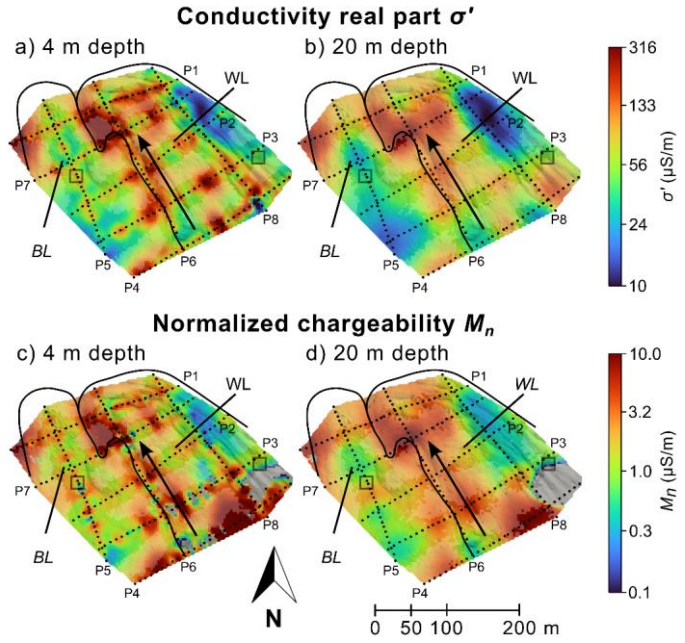

Figure A3C1: Conductivity real part (a and b) and normalized chargeability (c and d) visualized as slices parallel to the surface in two different depths. The edges of the black lobe (BL) and white lobe (WL) are indicated by black lines. Low sensitivity areas are displayed transparently, and the positions of electrodes are presented by black dots. Additionally, the direction of topography is indicated by a black arrow and the positions of tracer experiments by gray squares. The normalized chargeability refers to the difference between the bulk electrical conductivity at high and low frequency (2.5 and 0.5 Hz in our study, respectively), as presented in Equation 8.

Appendix D: Large-scale tracer experiment on the black lobe

Formatiert: Überschrift 1

Results of the large-scale tracer experiment on the black lobe are presented in Fig. D1.

hat formatiert: Schriftart: Nicht Fett

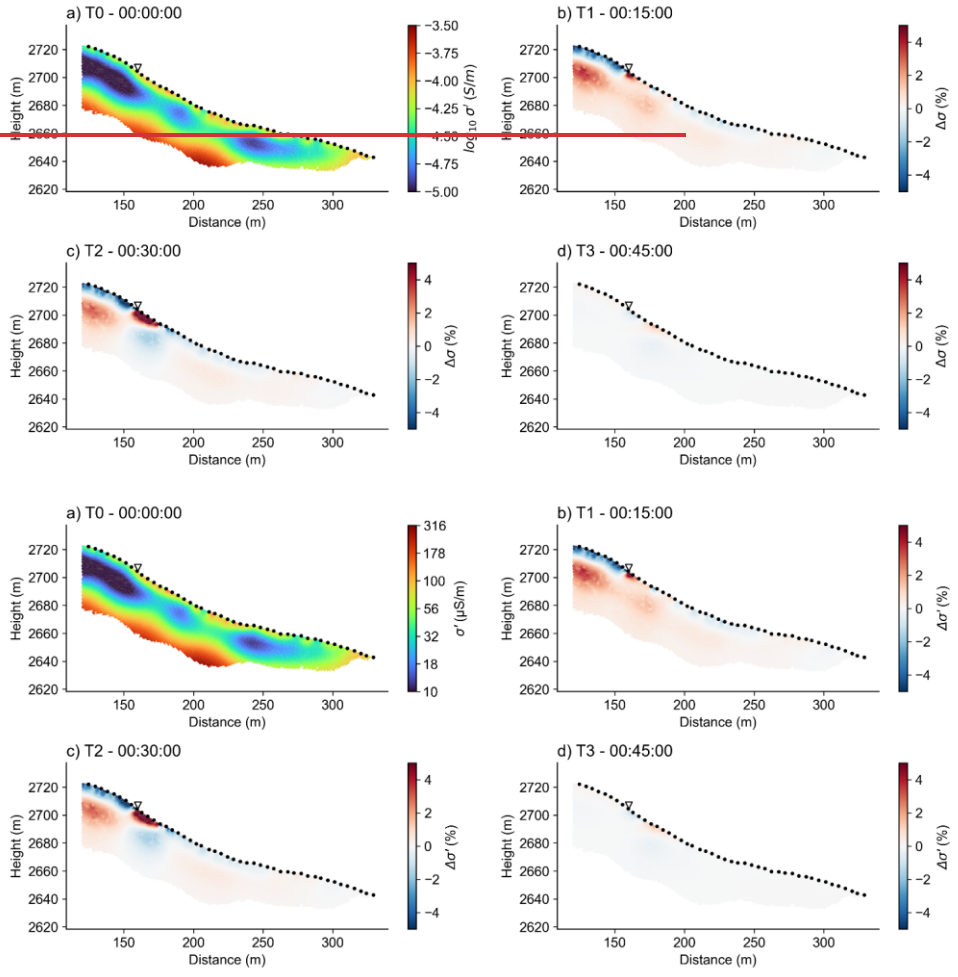

Figure A4D1: 2D conductivity inversion results of the baseline data for the large-scale tracer profile in the black lobe (a). Subplots b) to d) present the change of conductivity relative to the previous time step in % (linear scale). The

position of the tracer injection, at the surface, is indicated by a triangle, while the positions of electrodes are indicated by black dots.

Appendix E: Horizontal rock glacier movement 2020-2023

While we presented the horizontal rock glacier movement for the period 2022-2023 in Fig. 6, we show the mean velocity for a longer period (2020-2023) in Fig. E1

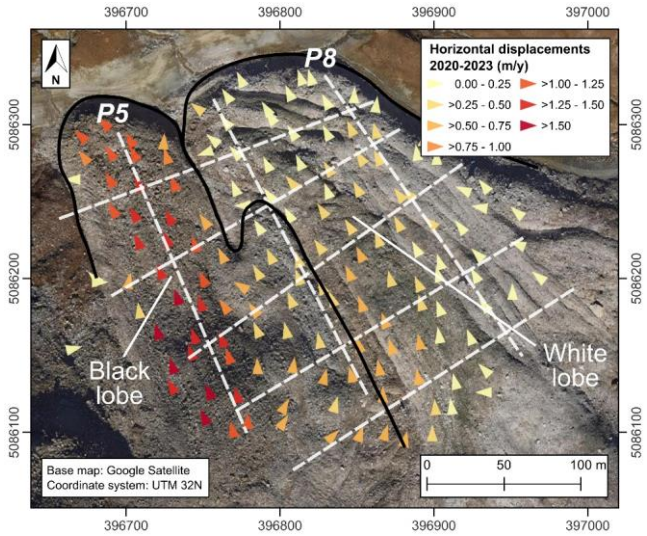

Figure A5E1: Horizontal displacements of the Gran Sometta rock glacier between 2020 and 2023. The direction of the arrows presents the direction of the rock glacier movement, while the color displays the velocity of the rock glacier in m/yr. The positions of the SIP profile are indicated by white dashed lines, while the front edge of the rock glacier and the border between the black and the white lobe are presented by a black line. Orthophoto: © Google Earth 2022.

Formatiert: Überschrift 1

hat formatiert: Schriftart: Nicht Fett

hat formatiert: Schriftart: Nicht Fett

hat formatiert: Schriftart: Nicht Fett

Formatiert: Links

Appendix F: Uncertainty of θ and K based on multi-frequency conductivity data

We estimated the standard deviation s of θ and K by applying error propagation law:

$$s_f = \sqrt{\sum_{i=1}^{n} \left(\frac{\partial f}{\partial x_i} s_{x_i}\right)^2}, \quad \text{(F17)}$$

where s_f is the standard deviation of the parameter f, s_{x_i} is the standard deviation of the parameter x_i, and i is the parameter number. For s_θ the partial derivatives are:

$$\frac{\partial \theta}{\partial \sigma_f} = -\frac{\left[\frac{1}{\sigma_f}\left(\sigma_\infty - \frac{M_n}{R}\right)\right]^{\frac{1}{m}}}{\sigma_f\, m} \quad \text{(F18)}$$

$$\frac{\partial \theta}{\partial R} = \frac{M_n\left[\frac{1}{\sigma_f}\left(\sigma_\infty - \frac{M_n}{R}\right)\right]^{\frac{1}{m}-1}}{\sigma_f\, m\, R^2} \quad \text{(f19)}$$

$$\frac{\partial \theta}{\partial m} = -\frac{\left[\frac{1}{\sigma_f}\left(\sigma_\infty - \frac{M_n}{R}\right)\right]^{\frac{1}{m}} log_{10}\left[\frac{1}{\sigma_f}\left(\sigma_\infty - \frac{M_n}{R}\right)\right]}{m^2} \quad \text{(F20)}$$

The derivatives for the CEC are:

$$\frac{\partial CEC}{\partial \theta} = -\frac{M_n\,(m-1)\,\theta^{-m}}{\rho_g\,\lambda} \quad \text{(F21)}$$

$$\frac{\partial CEC}{\partial m} = -\frac{M_n\,\theta^{1-m}\log_{10}\theta}{\rho_g\,\lambda} \quad \text{(F22)}$$

$$\frac{\partial CEC}{\partial \rho_g} = -\frac{M_n\,\theta^{1-m}}{\rho_g^2\,\lambda} \quad \text{(F23)}$$

$$\frac{\partial CEC}{\partial \lambda} = -\frac{M_n\,\theta^{1-m}}{\rho_g\,\lambda^2} \quad \text{(F24)}$$

The derivatives for the K are:

$$\frac{\partial K}{\partial k_0} = \frac{\theta^6}{\rho_g^2\, CEC^2}\frac{g\delta}{\mu} \quad \text{(F25)}$$

$$\frac{\partial K}{\partial \theta} = \frac{6\,k_0\,\theta^5}{\rho_g^2\, CEC^2}\frac{g\delta}{\mu} \quad \text{(F26)}$$

$$\frac{\partial K}{\partial \rho_g} = -\frac{2\,k_0\,\theta^6}{\rho_g^3\, CEC^2}\frac{g\delta}{\mu} \quad \text{(F27)}$$

Formatiert: Abstand Nach: 0 Pt., Zeilenabstand: einfach

hat formatiert: Schriftart: Englisch (Vereinigtes Königreich)

Formatiert: Block, Abstand Nach: 0 Pt.

Formatiert: Standard, Abstand Nach: 8 Pt.

hat formatiert: Schriftart: Englisch (Vereinigte Staaten)

$$\frac{\partial K}{\partial CEC} = -\frac{2\,k_0\,\theta^6}{\rho_g^2\,CEC^3}\frac{g\delta}{\mu} \quad \text{(F28)}$$

We used the following values and standard deviations for the parameters used above:

Parameter	Abbreviation	Absolute value	Standard deviation
Fluid conductivity	σ_f	0.01 S/m	0.005 S/m
Relation between M_n and σ_s	R	0.1	0.02
Cementation exponent	m	2.0	0.03
Grain density	ρ_g	2700 kg/m^3	100 kg/m^3
Apparent mobility of the counterions for the polarization	λ	3.0×10^{-10} m^2 s^{-1} V^{-1}	0.7×10^{-10} m^2 s^{-1} V^{-1}
Permeability fitting parameter	k_0	$10^{4.3}$	10^4

Table F1: Parameters used for the estimation of θ and K_s including absolute values and standard deviations used for the error propagation.

hat formatiert: Schriftart: Fett
Formatiert: Abstand Vor: 2 Pt., Nach: 2 Pt., Zeilenabstand: einfach, Keine Absatzkontrolle, Zeilennummern unterdrücken, Keine Silbentrennung
Formatierte Tabelle
Formatiert: Abstand Vor: 2 Pt., Nach: 2 Pt., Zeilenabstand: einfach, Keine Absatzkontrolle, Zeilennummern unterdrücken, Keine Silbentrennung
Formatiert: Abstand Vor: 2 Pt., Nach: 2 Pt., Zeilenabstand: einfach, Keine Absatzkontrolle, Zeilennummern unterdrücken, Keine Silbentrennung
Formatiert: Abstand Vor: 2 Pt., Nach: 2 Pt., Zeilenabstand: einfach, Keine Absatzkontrolle, Zeilennummern unterdrücken, Keine Silbentrennung
hat formatiert: Hochgestellt
Formatiert: Abstand Vor: 2 Pt., Nach: 2 Pt., Zeilenabstand: einfach, Keine Absatzkontrolle, Zeilennummern unterdrücken, Keine Silbentrennung
hat formatiert: Hochgestellt
Formatiert: Abstand Vor: 2 Pt., Nach: 2 Pt., Zeilenabstand: einfach, Keine Absatzkontrolle, Zeilennummern unterdrücken, Keine Silbentrennung
hat formatiert: Hochgestellt
hat formatiert: Hochgestellt
Formatiert: Abstand Vor: 2 Pt., Nach: 2 Pt., Zeilenabstand: einfach, Keine Absatzkontrolle, Zeilennummern unterdrücken, Keine Silbentrennung
hat formatiert: Schriftart: Fett
hat formatiert: Schriftart: Fett
hat formatiert: Schriftart: Fett
hat formatiert: Schriftart: Fett

Appendix G: Uncertainty of K based on tracer experiments

To investigate the sensitivity of the parameters ϕ and $\frac{\Delta H}{\Delta L}$ on the estimation of K based on v_p measurements are presented in Fig. G1.

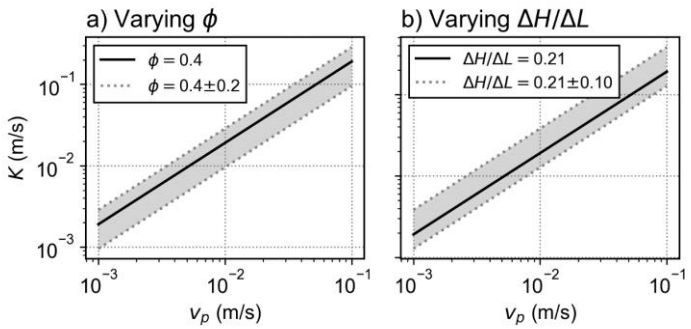

Figure G1: Effects of changing ϕ (a) and $\frac{\Delta H}{\Delta L}$ (b) on K. The black line symbolizes θ using $\phi = 0.4$ and $\frac{\Delta H}{\Delta L} = 0.21$, while the gray area limited by dashed lines shows the range of θ using $\pm 50\%$ of the values.

hat formatiert: Schriftart:
hat formatiert: Schriftart: Nicht Fett
Formatiert: Überschrift 1, Abstand Nach: 0 Pt.
hat formatiert: Schriftart: Nicht Fett
hat formatiert: Schriftart: Nicht Fett
hat formatiert: Schriftart: Nicht Fett
hat formatiert: Schriftart: Nicht Fett
Formatiert: Zentriert
hat formatiert: Schriftart: Fett

Data availability

The geophysical and kinematic data that support the findings of this study are available from the corresponding author upon request.

Author contributions

AFO and CM designed the experimental setup, all authors planned and coordinated the field logistics. CM and CH collected the geophysical data. CM processed the geophysical data, UMDC collected and processed the kinematic data. AFO, CH and CM interpreted the geophysical results, and all authors discussed the results. CM led the preparation of the draft, where all authors contributed actively, with major help from AFO and CH.

Competing interests

Some authors are members of the editorial board of The Cryosphere.

Acknowledgements

The authors are grateful to Sophia Keller, David Radlbauer, Elia Cornali and Ida Bürgermeister for their help in the collection of the geophysical data, to Federico Grosso and Michel Isabellon for their logistical support and help in the collection of the geophysical data during the field surveys, and to Theresa Maierhofer for the constructive comments on the manuscript. We are thankful to the cable car company Cervino S.p.A for the logistical support and to ARPA VdA for providing borehole temperature data. CM is thankful to ARPA VdA for hosting an Erasmus+ internship and to Erasmus+ for the financial support.

Financial support

This research is part of the project Tipping Points and Resilience of Mountain Permafrost under Increasing Frequency of Heat Waves (TREAT), which is financially supported by the Austrian Science Fund (FWF, grant no. I 6549-N).

References

Amschwand, D., Scherler, M., Hoelzle, M., Krummenacher, B., Haberkorn, A., Kienholz, C., and Gubler, H.: Surface heat fluxes at coarse blocky Murtèl rock glacier (Engadine, eastern Swiss Alps), The Cryosphere, 18, 2103–2139, https://doi.org/10.5194/tc-18-2103-2024, 2024.~~Amschwand, D., Scherler, M., Hoelzle, M., Krummenacher, B., Haberkorn, A., Kienholz, C., and Gubler, H.: Surface heat fluxes at coarse blocky Murtèl rock glacier (Engadine, eastern Swiss Alps), EGUsphere [preprint], https://doi.org/10.5194/egusphere-2023-2109, 2023.~~

Archie, G. E.: The Electrical Resistivity Log as an Aid in Determining Some Reservoir Characteristics, Petroleum Transactions of American Institute of Mining and Metallurgical Engineers (AIME), 146, 54–62, https://doi.org/10.2118/942054-G, 1942.

Arenson, L., Hoelzle, M., and Springman, S.: Borehole deformation measurements and internal structure of some rock glaciers in Switzerland, Permafrost Periglac., 13, 117–135, https://doi.org/10.1002/Ppp.414, 2002.

~~Auty, R. P., and Cole, R. H.: Dielectric properties of ice and solid D2O, J. Chem. Phys., 20, 1309–1314, https://doi.org/10.1063/1.1700726, 1952.~~

Barsch, D.: Rockglaciers: indicators for the present and former geoecology in high mountain environments, Springer, Berlin, 331 pp., 1996.

Bast, A., Kenner, R., and Phillips, M.: Short-term cooling, drying, and deceleration of an ice-rich rock glacier, The Cryosphere, 18, 3141–3158, https://doi.org/10.5194/tc-18-3141-2024, 2024.~~Bast, A., Kenner, R., and Phillips, M.: Short-term cooling, drying and deceleration of an ice-rich rock glacier, EGUsphere [preprint], https://doi.org/10.5194/egusphere-2024-269, 5 February 2024.~~

Bearzot, F., Garzonio, R., Di Mauro, B., Colombo, R., Cremonese, E., Crosta, G. B., Delaloye, R., Hauck, C., Morra Di Cella, U., Pogliotti, P., Frattini, P., and Rossini, M.: Kinematics of an Alpine rock glacier from multi-temporal UAV surveys and GNSS data, Geomorphology, 402, https://doi.org/10.1016/j.geomorph.2022.108116, 2022.

Bearzot, F., Colombo, N., Cremonese, E., Morra di Cella, U., Drigo, E., Caschetto, M., Basiricò, S., Crosta, G. B., Frattini, P., Freppaz, M., Pogliotti, P., Salerno, F., Brunier, A., Rossini, M.: Hydrological, thermal and chemical influence of an intact rock glacier discharge on mountain stream water, Sci. Total Environ., 876, https://doi.org/10.1016/j.scitotenv.2023.162777, 2023.

Beniston, M., Farinotti, D., Stoffel, M., Andreassen, L. M., Coppola, E., Eckert, N., Fantini, A., Giacona, F., Hauck, C., Huss, M., Huwald, H., Lehning, M., López-Moreno, J.-I., Magnusson, J., Marty, C., Morán-Tejéda, E., Morin, S., Naaim, M., Provenzale, A., Rabatel, A., Six, D., Stötter, J., Strasser, U., Terzago, S., and Vincent, C.: The European mountain cryosphere: a review of its current state, trends, and future challenges, The Cryosphere, 12, 759–794, https://doi.org/10.5194/tc-12-759-2018, 2018.

Benoit, S., Ghysels, G., Gommers, K., Hermans, T., Nguyen, F., Huysmans, M.: Characterization of Spatially Variable Riverbed Hydraulic Conductivity Using Electrical Resistivity Tomography and Induced Polarization, Hydrogeol. J., 27, 395–407, 2019.

Binley, A., and Kemna, A.: DC resistivity and induced polarization methods, in: Hydrogeophysics, edited by: Rubin, Y., and Hubbard, S. S., Springer, Dordrecht, Netherlands, 129–156, https://doi.org/10.1007/1-4020-3102-5_5, 2005.

Binley, A., and Slater, L.: Resistivity and Induced Polarization: Theory and Applications to the Near-surface Earth, Cambridge University Press, Cambridge, https://doi.org/10.1017/9781108685955.003, 2020.

Binley, A., Slater, L. D., Fukes, M., and Cassiani, G.: Relationship between spectral induced polarization and hydraulic properties of saturated and unsaturated sandstone, Water Resour. Res., 41, 12, https://doi.org/10.1029/2005WR004202, 2005.

Biskaborn, B. K., Smith, S. L., Noetzli, J., Matthes, H., Vieira, G., Streletskiy, D. A., Schoeneich, P., Romanovsky, V. E., Lewkowicz, A. G., Abramov, A., Allard, M., Boike, J., Cable, W. L., Christiansen, H. H., Delaloye, R., Diekmann, B., Drozdov, D., Etzelmüller, B., Grosse, G., Guglielmin, M., Ingeman-Nielsen, T., Isaksen, K., Ishikawa, M., Johansson, M., Johannsson, H., Joo, A., Kaverin, D., Kholodov, A., Konstantinov, P., Kröger, T., Lambiel, C., Lanckman, J.-P., Luo, D., Malkova, G., Meiklejohn, I., Moskalenko, N., Oliva, M., Phillips, M., Ramos, M., Sannel, A. B. K., Sergeev, D., Seybold, C., Skryabin, P., Vasiliev, A., Wu, Q., Yoshikawa, K., Zheleznyak, M., and Lantuit, H.: Permafrost is warming at a global scale, Nat. Commun., 10, 1–11, 2019.

Blanchy, G., Saneiyan, S., Boyd, J., McLachlan, P., and Binley, A.: ResIPy, an intuitive open source software for complex geoelectrical inversion/modeling, Comput. Geosci., 137, 104423, https://doi.org/10.1016/j.cageo.2020.104423, 2020.

Bodin, X., Thibert, E., Sanchez, O., Rabatel, A., and Jaillet, S.: Multi-Annual Kinematics of an Active Rock Glacier Quantified from Very High-Resolution DEMs: An Application-Case in the French Alps, Remote Sens., 10, 547, https://doi.org/10.3390/rs10040547, 2018.

Brighenti, S., Tolotti, M., Bruno, M. C., Wharton, G., Pusch, M. T., and Bertoldi, W.: Ecosystem shifts in Alpine streams under glacier retreat and rock glacier thaw: A review, Science of The Total Environment, 675, 542–559, https://doi.org/10.1016/j.scitotenv.2019.04.221, 2019.

Buchli, T., Merz, K., Zhou, X., Kinzelbach, W., and Springman, S. M.: Characterization and Monitoring of the Furggwanghorn Rock Glacier, Turtmann Valley, Switzerland: Results from 2010 to 2012, Vadose Zone J., 12, 1–15, https://doi.org/10.2136/vzj2012.0067, 2013.

Buchli, T., Kos, A., Limpach, P., Merz, K., Zhou, X., and Springman, S. M.: Kinematic investigations on the Furggwanghorn Rock Glacier, Switzerland, Permafrost Periglac., 29, 3–20, https://doi.org/10.1002/ppp.1968, 2018.

Burt, T. P., and Williams, P. J.: Hydraulic conductivity in frozen soils, Earth Surf. Process., 1, 349–360, https://doi.org/10.1002/esp.3290010404, 1976.

Camporese, M., Cassiani, G., Deiana, R., and Salandin, P.: Assessment of local hydraulic properties from electrical resistivity tomography monitoring of a three-dimensional synthetic tracer test experiment, Water Resour. Res.,47, W12508, https://doi.org/10.1029/2011WR010528, 2011.

hat formatiert: Absatz-Standardschriftart

Carman, P. C.: Permeability of saturated sands, soils and clays, J. Agric. Sci., 29, 263–273, 1939.

Cassiani, G., Bruno, V., Villa, A., Fusi, N., and Binley, A. M.: A saline trace test monitored via time-lapse surface electrical resistivity tomography, J. Appl. Geophys., 59, 244–259, https://doi.org/10.1016/j.jappgeo.2005.10.007, 2006.

Chambers, J. E., Ogilvy, R. D., Kuras, O., Cripps, J. C., and Meldrum, P. I.: 3D electrical imaging of known targets at a controlled environmental test site, Environ. Geology, 41, 6, 690–704, 2002.

Cicoira, A., Beutel, J., Faillettaz, J., and Vieli, A.: Water controls the seasonal rhythm of rock glacier flow, Earth Planet. Sc. Lett., 528, 115844, https://doi.org/10.1016/j.epsl.2019.115844, 2019.

Cicoira, A., Marcer, M., Gärtner-Roer, I., Bodin, X., Arenson, L. U., and Vieli, A.: A general theory of rock glacier creep based on in-situ and remote sensing observations, Permafrost Periglac. Process., 32, 139–153, 2021~~0~~.

Coperey, A., Revil, A., Abdulsamad, F., Stutz, B., Duvillard, P. A., and Ravanel, L.: Low-Frequency Induced Polarization of Porous Media Undergoing Freezing: Preliminary Observations and Modeling, J. Geophys. Res.-Sol. Ea., 124, 4523–4544, https://doi.org/10.1029/2018JB017015, 2019.

Del Siro, C., Scapozza, C., Perga, M.-E., Lambiel, C.: Investigating the origin of solutes in rock glacier springs in the Swiss Alps: A conceptual model, Front. Earth Sci., 11, https://doi.org/10.3389/feart.2023.1056305, 2023.

Delaloye, R., Lambiel, C., and Gärtner-Roer, I.: Overview of rock glacier kinematics research in the Swiss Alps: seasonal rhythm, interannual variations and trends over several decades, Geogr. Helvet., 65, 135–145, https://doi.org/10.5194/gh-65-135-2010, 2010.

Flores Orozco, A., Williams, K. H., and Kemna, A.: Time-lapse spectral induced polarization imaging of stimulated uranium bioremediation, Near Surf. Geophys., 11, 531–544, https://doi.org/10.3997/1873-0604.2013020, 2013.

Flores Orozco, A., Kemna, A., Binley, A., and Cassiani, G.: Analysis of time-lapse data error in complex conductivity imaging to alleviate anthropogenic noise for site characterization, Geophysics, 84, B181–B193, https://doi.org/10.1190/geo2017-0755.1, 2019.

Flores Orozco, A., Aigner, L., and Gallistl, J.: Investigation of cable effects in spectral induced polarization imaging at the field scale using multicore and coaxial cables, Geophysics, 86, E59–E75, https://doi.org/10.1190/geo2019-0552.1, 2021.

Flores Orozco, A., Steiner, M., Katona, T., Roser, N., Moser, C., Stumvoll, M. J., and Glade, T.: Application of induced polarization imaging across different scales to understand surface and groundwater flow at the Hofermuehle landslide, Catena, 219, 106612, https://doi.org/10.1016/j.catena.2022.106612, 2022.

Frohlich, R. K., Fisher, J. J., Summerly, E.: Electric-hydraulic conductivity correlation in fractured crystalline bedrock: Central Landfill, Rhode Island, USA, J. Appl. Geophys., 35, 249–259, 1996.

Geiger, S. T., Daniels, J. M., Miller, S. N., and Nicholas, J. W.: Influence of rock glaciers on stream hydrology in the La Sal Mountains, Utah, Arct. Antarct. Alp. Res., 46, 645–658, https://doi.org/10.1657/1938-4246-46.3.645, 2014.

Geuzaine, C., and Remacle, J.-F.: Gmsh: A 3-D finite element mesh generator with built-in pre- and post-processing facilities, Int. J. Numer. Meth. Engng., 79, 1309–1331, https://doi.org/10.1002/nme.2579, 2009.

Giardino, R., Regmi, N., and Vitek, J.: Rock glaciers, in: Encyclopedia of snow, ice and glaciers, edited by: Singh, V. P., Singh, P., and Haritashya U. K., Springer, Dordrecht, Netherlands, 943–948, https://doi.org/10.1007/978-90-481-2642-2_453, 2011.

~~Grimm, R. E., and Stillman, D. E.: Field test of detection and characterisation of subsurface ice using broadband spectral induced polarisation, Permafr. Periglac. Process., 26, 28–38, https://doi.org/10.1002/ppp.1833, 2015.~~

Haeberli, W.: Creep of mountain permafrost: internal structure and flow of alpine rock glaciers, Mitteilungen der Versuchsanstalt für Wasserbau, Hydrol. Und Gaziologie an der ETH Zurich, Zurich, 5–142,1985.

Haeberli, W., Hallet, B., Arenson, L., Elconin, R., Humlum, O., Kääb, A., Kaufmann, V., Ladanyi, B., Matsuoka, N., Springman, S., and Mühll, D. V.: Permafrost creep and rock glacier dynamics, Permafrost Periglac., 17, 189–214, https://doi.org/10.1002/ppp.561, 2006.

Haeberli, W., Schaub, Y., and Huggel, C.: Increasing risks related to landslides from degrading permafrost into new lakes in de-glaciating mountain ranges, Geomorphology, 293, 405–417, 2017.

Halla, C., Blöthe, J. H., Tapia Baldis, C., Trombotto Liaudat, D., Hilbich, C., Hauck, C., and Schrott, L.: Ice content and interannual water storage changes of an active rock glacier in the dry Andes of Argentina, The Cryosphere, 15, 1187–1213, https://doi.org/10.5194/tc-15-1187-2021, 2021

Harrington, J. S., Mozil, A., Hayashi, M., and Bentley, L. R.: Groundwater flow and storage processes in an inactive rock glacier, Hydrol. Process., 32, 3070–3088, 2018.

Hauck, C., Böttcher, M., and Maurer, H.: A new model for estimating subsurface ice content based on combined electrical and seismic data sets, The Cryosphere, 5, 453–468, https://doi.org/10.5194/tc-5-453-2011, 2011.

Hördt, A., Druiventak, A., Blaschek, R., Binot, F., Kemna, A., Kreye, P., and Zisser, N.: Case histories of hydraulic conductivity estimation with induced polarization at the field scale, Near Surface Geophysics, 7, 529– 545, https://doi.org/10.3997/1873-0604.2009035, 2009.

Ikeda, A., Matsuoka, N., and Kääb, A.: Fast deformation of perennially frozen debris in a warm rock glacier in the Swiss Alps: An effect of liquid water, J. Geophys. Res.-Earth, 113, F01021, https://doi.org/10.1029/2007jf000859, 2008.

Jones, D. B., Harrison, S., Anderson, K., and Betts, R. A.: Mountain rock glaciers contain globally significant water stores, Sci. Rep.-UK, 8, 2834, https://doi.org/10.1038/s41598-018-21244-w, 2018.

Jones, D. B., Harrison, S., Anderson, K., and Whalley, W. B.: Rock glaciers and mountain hydrology: A review, Earth-Sci. Rev., 193, 66–90, https://doi.org/10.1016/j.earscirev.2019.04.001, 2019.

Kääb, A., Frauenfelder, R., and Roer, I.: On the response of rockglacier creep to surface temperature increase, Global Planet. Change, 56, 172–187, https://doi.org/10.1016/j.gloplacha.2006.07.005, 2007.

Kellerer-Pirklbauer, A., Bodin, X., Delaloye, R., Lambiel, C., Gärtner-Roer, I., Bonnefoy-Demongeot, M., Carturan, L., Damm, B., Eulenstein, J., Fischer, A., Hartl, L., Ikeda, A., Kaufmann, V., Krainer, K., Matsuoka, N., Morra Di Cella, U., Noetzli, J., Seppi, R., Scapozza, C., Schoeneich, P., Stocker-Waldhuber, M., Thibert, E., and Zumiani, M.: Acceleration and

interannual variability of creep rates in mountain permafrost landforms (rock glacier velocities) in the European Alps in 1995–2022, Environ. Res. Lett., 19, 034022, https://doi.org/10.1088/1748-9326/ad25a4, 2024.

Kemna, A., Vanderborght, J., Kulessa, B., and Vereecken, H.: Imaging and characterisation of subsurface solute transport using electrical resistivity tomography (ERT) and equivalent transport models, J. Hydrol., 267, 125–146, https://doi.org/10.1016/s0022-1694(02)00145-2, 2002.

Kemna, A., Binley, A., and Slater, L.: Crosshole IP imaging for engineering and environmental applications, Geophysics, 69, 97–107, https://doi.org/10.1190/1.1649379, 2004.

Kenner, R., Phillips, M., Beutel, J., Hiller, M., Limpach, P., Pointner, E., and Volken, M.: Factors Controlling Velocity Variations at Short-Term, Seasonal and Multiyear Time Scales, Ritigraben Rock Glacier, Western Swiss Alps, Permafrost Periglac., 28, 675–684, https://doi.org/10.1002/ppp.1953, 2017.

Kenner, R., Pruessner, L., Beutel, J., Limpach, P., and Phillips, M.: How rock glacier hydrology, deformation velocities and ground temperatures interact: Examples from the Swiss Alps, Permafr. Periglac. Process., 31, 3–14, https://doi.org/10.1002/ppp.2023, 2019.

Kneisel, C., Hauck, C., Fortier, R., and Moorman, B.: Advances in geophysical methods for permafrost investigations, Permafrost Periglac., 19, 157–178, https://doi.org/10.1002/ppp.616, 2008.

Kozeny, J.: Über kapillare Leitung des Wassers im Boden, Sitzungsber. Akad. Wiss. Wien Math. Naturwiss. Kl. Abt. 1, 136, 271–306, 1927.

Krainer, K., and Mostler, W.: Hydrology of active rock glaciers: Examples from the Austrian Alps, Arct. Antarct. Alp. Res., 34, 142–149, https://doi.org/10.2307/1552465, 2002.

Krainer, K., Mostler, W., and Spötl, C.: Discharge from active rock glaciers, Austrian Alps: a stable isotope approach, Austrian J. Earth Sci., 100, 102–112, 2007.

Krainer, K., Bressan, D., Dietre, B., Haas, J. N., Hajdas, I., Lang, K., Mair, V., Nickus, U., Reidl, D., Thies, H., and Tonidandel, D.: A 10 300-year-old permafrost core from the active rock glacier Lazaun, southern Ötztal Alps (South Tyrol, northern Italy), Quaternary Res., 83, 324–335, https://doi.org/10.1016/j.yqres.2014.12.005, 2015.

Krautblatter, M., Funk, D., and Günzel, F. K.: Why permafrost rocks become unstable: a rock–ice-mechanical model in time and space, Earth Surf. Process. Landf., 38, 876–887, https://doi.org/10.1002/esp.3374, 2013.

LaBrecque, D. J., Miletto, M., Daily, W., Ramirez, A., and Owen, E.: The effects of noise on Occam's inversion of resistivity tomography data, Geophysics, 61, 2, 538–548, https://doi.org/10.1190/1.1443980, 1996.

Leroy, P., Revil, A., Kemna, A., Cosenza, P., and Ghorbani, A.: Complex conductivity of water-saturated packs of glass beads, J. Colloid Interfac., 321, 103–117, https://doi.org/10.1016/j.jcis.2007.12.031, 2008.

~~Limbrock, J. K., Weigand, M., and Kemna, A.: Improved thermal characterization of alpine permafrost sites by broadband SIP measurements, EGU General Assembly 2020, Online, 4–8 May 2020, EGU2020-20081, https://doi.org/10.5194/egusphere-egu2020-20081, 2020.~~

Luethi, R., Phillips, M., Lehning, M.: Estimating Non-Conductive Heat Flow Leading to Intra-Permafrost Talik Formation at the Ritigraben Rock Glacier (Western Swiss Alps), Permafrost and Periglac. Process., 28, 183–194, https://doi.org/10.1002/ppp.1911, 2017.

Maierhofer, T., Hauck, C., Hilbich, C., Kemna, A., and Flores-Orozco, A.: Spectral induced polarization imaging to investigate an ice-rich mountain permafrost site in Switzerland, The Cryosphere, 16, 1903–1925, https://doi.org/10.5194/tc-16-1903-2022, 2022.

Maierhofer, T., Flores Orozco, A., Roser, N., Limbrock, J. K., Hilbich, C., Moser, C., Kemna, A., Drigo, E., Morra di Cella, U., and Hauck, C.: Spectral induced polarization imaging to monitor seasonal and annual dynamics of frozen ground at a mountain permafrost site in the Italian Alps, The Cryosphere, 18, 3383–3414, https://doi.org/10.5194/tc-18-3383-2024, 2024.

Mao, D., Revil, A., and Hinton, J.: Induced polarization response of porous media with metallic particles — Part 4: Detection of metallic and nonmetallic targets in time-domain induced polarization tomography, Geophysics, 81, 4, D359–D375, https://doi.org/10.1190/GEO2015-0480.1, 2016.

Marcer, M., Cicoira, A., Cusicanqui, D., Bodin, X., Echelard, T., Obregon, R., and Schoeneich, P.: Rock glaciers throughout the French Alps accelerated and destabilised since 1990 as air temperatures increased, Commun. Earth Environ., 2, 81, https://doi.org/10.1038/s43247-021-00150-6, 2021.

Mollaret, C., Hilbich, C., Pellet, C., Flores-Orozco, A., Delaloye, R., and Hauck, C.: Mountain permafrost degradation documented through a network of permanent electrical resistivity tomography sites, The Cryosphere, 13, 2557–2578, https://doi.org/10.5194/tc-13-2557-2019, 2019.

~~Mollaret, C., Wagner, F. M., Hilbich, C., Scapozza, C., and Hauck, C.: Petrophysical Joint Inversion Applied to Alpine Permafrost Field Sites to Image Subsurface Ice, Water, Air, and Rock Contents, Front. Earth Sci., 8, 1–25, https://doi.org/10.3389/feart.2020.00085, 2020.~~

Moser, C., Binley, A., and Flores Orozco, A.: 3D electrode configurations for spectral induced polarization surveys of landfills, Waste Management, 169, 208–222, https://doi.org/10.1016/j.wasman.2023.07.006, 2023.

~~Mudler, J., Hördt, A., Kreith, D., Sugand, M., Bazhin, K., Lebedeva, L., and Radić, T.: Broadband spectral induced polarization for the detection of Permafrost and an approach to ice content estimation – a case study from Yakutia, Russia, The Cryosphere, 16, 4727–4744, https://doi.org/10.5194/tc-16-4727-2022, 2022.~~

Müller, J., Vieli, A., and Gärtner-Roer, I.: Rock glaciers on the run – understanding rock glacier landform evolution and recent changes from numerical flow modeling, The Cryosphere, 10, 2865–2886, https://doi.org/10.5194/tc-10-2865-2016, 2016.

Noetzli, J., Arenson, L. U., Bast, A., Beutel, J., Delaloye, R., Farinotti, D., Gruber, S., Gubler, H., Haeberli, W., Hasler, A., Hauck, C., Hiller, M., Hoelzle, M., Lambiel, C., Pellet, C., Springman, S. M., Vonder Muehll, D., and Phillips, M.: Best Practice for Measuring Permafrost Temperature in Boreholes Based on the Experience in the Swiss Alps, Front. Earth Sci., 9, 607875, https://doi.org/10.3389/feart.2021.607875, 2021.

Pavoni, M., Boaga, J., Carrera, A., Zuecco, G., Carturan, L., and Zumiani, M.: Brief communication: Mountain permafrost acts as an aquitard during an infiltration experiment monitored with electrical resistivity tomography time-lapse measurements, The Cryosphere, 17, 1601–1607, https://doi.org/10.5194/tc-17-1601-2023, 2023b.

Pavoni, M., Boaga, J., Wagner, F. M., Bast, A., and Phillips, M.: Characterization of rock glaciers environments combining structurally coupled and petrophysically coupled joint inversions of electrical resistivity and seismic refraction datasets, Journal of Applied Geophysics, 215, 105097, https://doi.org/10.1016/j.jappgeo.2023.105097, 2023a.

Perri, M. T., Cassiani, G., Gervasio, I., Deiana, R., and Binley, A.: A saline tracer test monitored via both surface and cross-borehole electrical resistivity tomography: Comparison of time-lapse results, J. Appl. Geophys., 79, 6–16, https://doi.org/10.1016/j.jappgeo.2011.12.011, 2012.

Phillips, M., Buchli, C., Weber, S., Boaga, J., Pavoni, M., and Bast, A.: Brief communication: Combining borehole temperature, borehole piezometer and cross-borehole electrical resistivity tomography measurements to investigate seasonal changes in ice-rich mountain permafrost, The Cryosphere, 17, 753–760, https://doi.org/10.5194/tc-17-753-2023, 2023.

Pourrier, J., Jourde, H., Kinnard, C., Gascoin, S., and Monnier, S.: Glacier meltwater flow paths and storage in a geomorphologically complex glacial foreland: The case of the Tapado glacier, dry Andes of Chile (30∘ S), J. Hydrol., 519, 1068–1083, https://doi.org/10.1016/j.jhydrol.2014.08.023, 2014.

Pruessner, L., Huss, M., Phillips, M., and Farinotti, D.: A Framework for Modeling Rock Glaciers and Permafrost at the Basin-Scale in High Alpine Catchments, J. Adv. Model. Earth Syst., 13, e2020MS002361, https://doi.org/10.1029/2020MS002361, 2021.

Rangecroft, S., Harrison, S., and Anderson, K.: Rock Glaciers as Water Stores in the Bolivian Andes: An Assessment of Their Hydrological Importance, Arct. Antarct. Alp. Res., 47, 89–98, https://doi.org/10.1657/AAAR0014-029, 2015.

Revil, A.: Effective conductivity and permittivity of unsaturated porous materials in the frequency range 1 mHz–1GHz, Water Resour. Res., 49, 306–307, https://doi.org/10.1029/2012WR012700, 2013a.

Revil, A.: On charge accumulation in heterogeneous porous rocks under the influence of an external electric field, Geophysics, 78, 4, D271–D291, https://doi.org/10.1190/GEO2012-0503.1, 2013b.

Revil, A., and Florsch, N.: Determination of permeability from spectral induced polarization in granular media, Geophys. J. Int., 181, 1480–1498, https://doi.org/10.1111/j.1365-246x.2010.04573.x, 2010.

Revil, A., Binley, A., Mejus, L., and Kessouri, P.: Predicting permeability from the characteristic relaxation time and intrinsic formation factor of complex conductivity spectra, Water Resour. Res., 51, 6672–6700, https://doi.org/10.1002/2015WR017074, 2015.

Revil, A., Breton, M. L., Niu, Q., Wallin, E., Haskins, E., Thomas, D. M.: Induced polarization of volcanic rocks—1. Surface versus quadrature conductivity, Geophys. J. Int., 208, 2, 826–844, https://doi.org/10.1093/gji/ggw444, 2017a.

Revil, A., Breton, M. L., Niu, Q., Wallin, E., Haskins, E., and Thomas, D. M.: Induced polarization of volcanic rocks.—2. Influence of pore size and permeability, Geophys. J. Int., 208, 2, 814–825, https://doi.org/10.1093/gji/ggw382, 2017b.

Revil, A., Coperey, A., Shao, Z., Florsch, N., Fabricius, I. L., Deng, Y., Delsman, J. R., Pauw, P.S., Karaoulis, M., de Louw, P. G. B., van Baaren, E. S., Dabekaussen, W., Menkovic, A., and Gunnink, J. L.: Complex conductivity of soils, Water Resour. Res., 53, 8, 7121–7147, 2017c.

Revil, A., Soueid, A., Coperey, A., Ravanel, L., Sharma, R., and Panwar, N.: Induced polarization as a tool to characterize shallow landslides, J. Hydrol., 589, 125369, https://doi.org/10.1016/j.jhydrol.2020.125369, 2020.

Revil, A., Schmutz, M., Abdulsamad, F., Balde, A., Beck, C., Ghorbani, A., and Hubbard, S.: Field-scale estimation of soil properties from spectral induced polarization tomography, Geoderma, 403, 115380, https://doi.org/10.1016/j.geoderma.2021.115380, 2021.

Roer, I., Haeberli, W., Avian, M., Kaufmann, V., Delaloye, R., Lambiel, C., and Kääb, A.: Observations and considerations on destabilizing active rock glaciers in the European Alps, in: Proceedings of the 9th International Conference on Permafrost, Fairbanks, Alaska, 1505–1510, 2008.

Rogger, M., Chirico, G. B., Hausmann, H., Krainer, K., Brückl, E., Stadler, P., and Blöschl, G.: Impact of mountain permafrost on flow path and runoff response in a high alpine catchment, Water Resour. Res., 53, 1288–1308, https://doi.org/10.1002/2016WR019341, 2017.

~~Seigel, H. O.: Mathematical formulation and type curves for induced polarization, Geophysics, 24, 3, 547–565, https://doi.org/10.1190/1.1438625, 1959.~~

Singha, K., and Gorelick, S. M.: Saline tracer visualized with three-dimensional electrical resistivity tomography: Field-scale spatial moment analysis, Water Resour. Res., 41, W05023, https://doi.org/10.1029/2004WR003460, 2005.

Slater, L.: Near surface electrical characterization of hydraulic conductivity: From petrophysical properties to aquifer geometries—A review, Surv. Geophys., 28, 169–197, 2007.

Slater, L., Barrash, W., Montrey, J., and Binley, A.: Electrical-hydraulic relationships observed for unconsolidated sediments in the presence of a cobble framework, Water Resources Research, 50, 5721–5742, https://doi.org/10.1002/2013WR014631, 2014.

Soueid Ahmed, A., Revil, A., Abdulsamad, F., Steck, B., Vergniault, C., and Guihard, V.: Induced polarization as a tool to non-intrusively characterize embankment hydraulic properties, Eng. Geol., 271, 10560, https://doi.org/10.1016/j.enggeo.2020.105604, 2020.

~~Steiner, M., Wagner, F. M., Maierhofer, T., Schöner, W., and Flores Orozco, A.: Improved estimation of ice and water contents in alpine permafrost through constrained petrophysical joint inversion: The Hoher Sonnblick case study, Geophysics, 85, WB119–WB133, https://doi.org/10.1190/geo2020-0592.1, 2021~~

Stillman, D. E., Grimm, R. E., and Dec, S. F.: Low-Frequency Electrical Properties of Ice – Silicate Mixtures, J. Phys. Chem., 114, 6065–6073, https://doi.org/10.1021/jp9070778, 2010.

Urish, D.: Electrical resistivity-hydraulic conductivity relationships in glacial outwash aquifers, Water Resour. Res., 17, 5, 1401–1408, 1981.

Van Genuchten, M. T.: A Closed-form Equation for Predicting the Hydraulic Conductivity of Unsaturated Soils, Soil Sci. Soc. Am. J., 44, 892–898, https://doi.org/10.2136/sssaj1980.03615995004400050002x, 1980.

Van Voorhis, G. D., Nelson, P. H., and Drake, T. L.: Complex resistivity spectra of porphyry copper mineralization, Geophysics, 38, 1, 49–60, https://doi.org/10.1190/1.1440333, 1973.

Vinegar, H. J., and Waxman, M. H.: Induced polarization of shaly sands, Geophysics, 49, 8, 1267–1287, 1984.

~~Wagner, F. M., Mollaret, C., Günther, T., Kemna, A., and Hauck, C.: Quantitative imaging of water, ice and air in permafrost systems through petrophysical joint inversion of seismic refraction and electrical resistivity data, Geophys. J. Int., 219, 1866–1875, 2019.~~

Wagner, T., Kainz, S., Helfricht, K., Fischer, A., Avian, M., Krainer, K., and Winkler, G.: Assessment of liquid and solid water storage in rock glaciers versus glacier ice in the Austrian Alps, Sci. Total Environ., 800, 149593, https://doi.org/10.1016/j.scitotenv.2021.149593, 2021.

Weller, A., Slater, L., Binley, A., Nordsiek, S., and Xu, S.: Permeability prediction based on induced polarization: Insights from measurements on sandstone and unconsolidated samples spanning a wide permeability range, Geophysics, 80, D161–D173, 2015.

Weller, A., Slater, L., and Nordsiek, S.: On the relationship between induced polarization and surface conductivity: Implications for petrophysical interpretation of electrical measurements, Geophysics, 78, 5, D315–D325, https://doi.org/10.1190/GEO2013-0076.1, 2013.

Western, A. W., Blöschl, G., and Grayson, R. B.: Toward capturing hydrologically significant connectivity in spatial patterns, Water Resour. Res., 37, 1, 83–97, https://doi.org/10.1029/2000WR900241, 2001.

Winkler, G., Wagner, T., Pauritsch, M., Birk, S., Kellerer-Pirklbauer, A., Benischke, R., Leis, A., Morawetz, R., Schreilechner, M. G., and Hergarten, S.: Identification and assessment of groundwater flow and storage components of the relict Schöneben Rock Glacier, Niedere Tauern Range, Eastern Alps (Austria), Hydrogeol. J., 24, 937–953, https://doi.org/10.1007/s10040-015-1348-9, 2016.

Wirz, V., Beutel, J., Gruber, S., Gubler, S., and Purves, R. S.: Estimating velocity from noisy GPS data for investigating the temporal variability of slope movements, Nat. Hazards Earth Syst. Sci., 14, 2503–2520, https://doi.org/10.5194/nhess-14-2503-2014, 2014.

Wirz, V., Gruber, S., Purves, R. S., Beutel, J., Gartner-Roer, I., Gubler, S., and Vieli, A.: Short-term velocity variations at three rock glaciers and their relationship with meteorological conditions, Earth Surf. Dynam., 4, 103–123, https://doi.org/10.5194/esurf-4-103-2016, 2016.

Waxman, M. H., and Smits, L. J. M.: Electrical conductivities in oil-bearing shaly sands, Society of Petroleum Engineers Journal, 8, 107–122, 1968.

Zenklusen Mutter, E., Phillips, M.: Active Layer Characteristics At Ten Borehole Sites In Alpine Permafrost Terrain, Switzerland, Permafrost and Periglac. Process., 23, 138–151, 2012.

Zorin, N., and Ageev, D.: Electrical properties of two-component mixtures and their application to high-frequency IP exploration of permafrost, Near Surf. Geophys., 15, 603–613, 2017.